2009

Numerical investigation of synthetic jet ejector (SJE) performance

Feng Lin
University of Windsor

NUMERICAL INVESTIGATION OF SYNTHETIC JET EJECTOR (SJE) PERFORMANCE

by

FENG LIN

A Thesis

Submitted to the Faculty of Graduate Studies through

Mechanical, Automotive and Materials Engineering

in Partial Fulfillment of the Requirements for

the Degree of Master of Applied Science at the

University of Windsor

Windsor, Ontario, Canada

2009

Your file Votre référence
ISBN: 978-0-494-57626-7
Our file Notre référence
ISBN: 978-0-494-57626-7

AUTHOR'S DECLARATION OF ORIGINALITY

I hereby certify that I am the sole author of this thesis and that no part of this thesis has been published or submitted for publication.

I certify that, to the best of my knowledge, my thesis does not infringe upon anyone's copyright nor violate any proprietary rights and that any ideas, techniques, quotations, or any other material from the work of other people included in my thesis, published or otherwise, are fully acknowledged in accordance with the standard referencing practices. Furthermore, to the extent that I have included copyrighted material that surpasses the bounds of fair dealing within the meaning of the Canada Copyright Act, I certify that I have obtained a written permission from the copyright owner(s) to include such material(s) in my thesis and have included any copies of such copyright clearances in an appendix.

I declare that this is a true copy of my thesis, including my final revisions, as approved by my thesis committee and the Graduate Studies office, and that this thesis has not been submitted for a higher degree to any other University or Institution.

ABSTRACT

The performance of a synthetic jet ejector (SJE) has been investigated numerically using Computational Fluid Dynamics (CFD). A parametric study was conducted and combined with a search procedure to determine the conditions for optimum volume flow rate through the device. Active parameters such as input driving frequency and input velocity amplitude as well as passive parameters describing the ejector geometry, such as the orifice diameter, shroud diameter, and shroud length were considered.

Results show that the SJE has an optimum operating condition. The optimum orifice diameter is theoretically the same as the actuator diameter, which is 0.8 times the shroud diameter. The optimum shroud length is 4 times the shroud diameter. The corresponding Strouhal number and Reynolds number are 0.323 and 20,000, respectively.

The use of this particular SJE configuration to replace the ventilation fan in an automotive seat cooling application is also considered. The SJE for this application has an orifice diameter of 16 mm, a shroud diameter of 20 mm, and a shroud length of 80 mm, with a driving frequency of 250 Hz, and input velocity amplitude of 15.5 m/s. It is shown that 10 such devices operating in parallel would be required to attain the same ventilation as existing fans.

DEDICATION

This thesis is dedicated to

My parents: Ying Bao Lei and Bin Han Lin

My wife: Kwai Chung Tam

and

My children: Vincent Lin and Vivian Lin

ACKNOWLEDGEMENT

I would like to express my sincere gratitude to my supervisor, Dr. Rankin, for giving me this wonderful opportunity to work on this project, for his professional guidance, insight, and patience throughout my graduate study. I also would like to thank Dr. Kaloni for his encouragement, and support.

I would like to express my sincere thanks to Dr. Sokolowski, Dr. Barron and Mr. Colja for being my thesis committee members, for their helpful suggestions and valuable time to review my thesis. I also would like to extend my thanks to Dr. Minaker for acting as the chair of my defense.

I am indebted to my family for their unconditional love and support. Special thanks to my sister, Ling.

I also would like to thank my colleagues, Anirban, Hoda, Nancy, Shelagh and everyone involved in this project for sharing their knowledge with me.

Acknowledgement also goes to Leggett & Platt Automotive and the Ontario Centre of Excellence (OCE) for their financial support. Sincere thanks to SHARCNET for the use of certain computing resources.

TABLE OF CONTENTS

LIST OF TABLES

LIST OF FIGURES

NOMENCLATURE

A	average cell area
A'	dimensionless average cell area
A_p	primary inlet area
A_s	secondary inlet area
A_t	total outlet area
C_e	entrainment coefficient
d	synthetic jet orifice diameter
D	synthetic jet actuator diameter
D_e	synthetic jet ejector shroud diameter
Eu	Euler number for general jet
Eu_e	synthetic jet ejector Euler number
f	synthetic jet diaphragm driving frequency
f_a	cluster factor
h	synthetic jet actuator exit width
H	extent of calculation domain in y direction
k	integer between 1 and n
L_e	synthetic jet ejector shroud length
L_o	stroke length
M	number of cells along y axis

Ma	Mach number
M_p	mass flow rate at primary inlet
M_s	mass flow rate at secondary inlet
$\dot{M}_e$	entrained mass flow rate up to position x
$\Delta\dot{M}_e$	entrained mass flow rate difference between any two locations
$\dot{M}_j$	jet mass flow rate at the orifice
n	number of time steps per cycle
N	number of cells along x axis
Δp	area-average pressure drop across the SJE
Re	Reynolds number for general jet
Re_e	synthetic jet ejector Reynolds number
Re_{U_0}	synthetic jet Reynolds number
S	Stokes number
St	Strouhal number
St_e	synthetic jet ejector Strouhal number
Δt	time step size
T	synthetic jet actuator diaphragm vibration period
U	time-averaged synthetic jet centreline velocity
U_{cl}	centreline velocity
U_0	synthetic jet velocity

$\overline{U}_p$	period area-average primary inlet velocity
$\overline{U}_s$	period area-average secondary inlet velocity
$\overline{U}_t$	period area-average outlet (total) velocity
V	area-average velocity at the exit
V_A	synthetic jet actuator orifice area-average velocity amplitude
V_p	synthetic jet actuator orifice area-average velocity
V_s	synthetic jet ejector secondary inlet area-average velocity
W	extent of calculation domain in x direction
x	axial distance from orifice exit plane
Δx	calculation domain first column cell dimension in x direction
y	radial distance from axis
Δy	calculation domain first column cell dimension in y direction

Greek Letters

ρ	air density
ρ_j	jet density at the orifice
ρ_s	density of surrounding atmosphere
μ	air dynamic viscosity
υ	air kinematic viscosity

ABBREVIATIONS

CFD	Computational Fluid Dynamics
CPU	Central Processing Unit
DNS	Direct Numerical Simulation
MEMS	Micro-electromechanical System
SI	Secondary Inlet
SJ	Synthetic Jet
SJA	Synthetic Jet Actuator
SJE	Synthetic Jet Ejector
TSPC	Time Steps per Cycle
UDF	User Defined Function

CHAPTER 1

INTRODUCTION

A jet is a stream of fluid forced through an opening under pressure into a surrounding medium. The jet is called submerged when the jet fluid is the same as the surrounding medium, such as the jet produced by a hair dryer. If the fluids are different, the jet is referred to as non-submerged. One example of a non-submerged jet is the water jet from a garden hose. Steady jet refers to a jet with constant quantities (such as velocity and pressure) at any given point in space, while those of an unsteady jet vary with time. A free jet is one with exit open to the atmosphere. When the surrounding medium is physically constrained within a device, such as a shroud, it becomes a confined jet.

1.1 Synthetic Jets

A free synthetic jet (SJ) is produced by the interaction of vortices that are typically formed by alternating momentary ejection and suction of fluid across an orifice such that the net mass flux is zero [4]. It is an unsteady jet. A synthetic jet actuator (SJA) is a device used to produce a SJ. It typically consists of a cavity, oscillating diaphragm and small opening on one side. This study focuses on a submerged free synthetic air jet with a round orifice for its geometrical simplicity. As shown in Figure 1.1a, the diaphragm basically bends in and out of the cavity during the cycle, which can be divided into an ejection and suction phase. During the ejection phase, the diaphragm bends into the cavity from its lower position. Air is pushed out, forms a vortex sheet and then rolls into a vortex ring at the edge. When the diaphragm starts moving back from its upper position and goes into the suction phase, the vortex separates and moves away from the edge with a self-induced velocity, and the surrounding air is sucked back into the cavity. As the vortex moves downstream, it breaks down into vortices of smaller scales. The interactions of the series of vortices are what form the SJ. During a cycle, a vortex ring is created and the net mass flow rate is zero at the exit plane. When the opening is

two-dimensional, one pair of vortices is formed during each cycle. Earlier research [23] has shown that, at a low Reynolds number, a SJ from an axisymmetric orifice is easier to form than one from a two-dimensional slot.

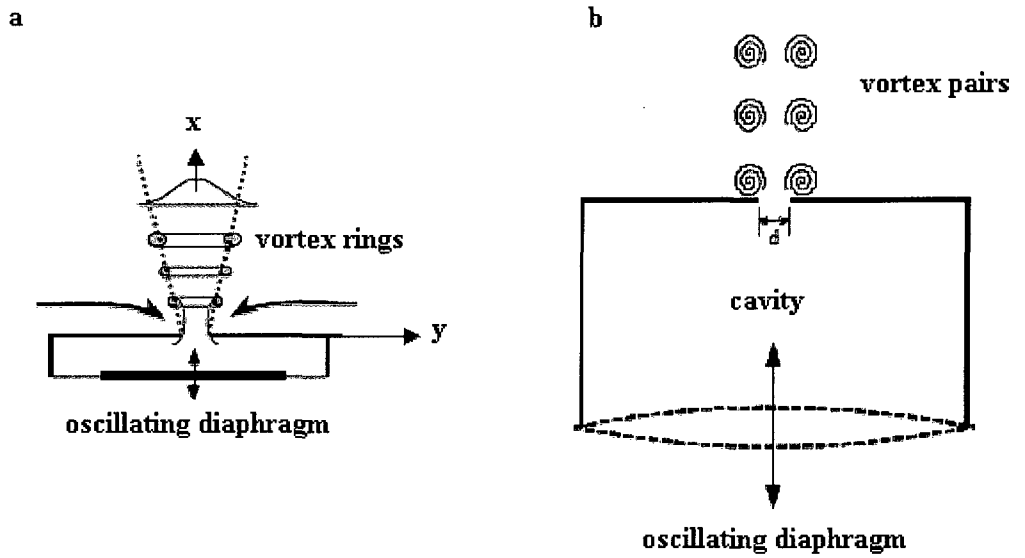

Figure 1.1 Synthetic jets formed by (a) round orifice, and (b) two-dimensional slot [17].

The primary advantage of a SJ is that it has a zero net mass flux at the exit. It only transfers momentum to the surroundings. It is easy to implement because there is no need to install piping or an extra flow source. Over the years, SJs have been applied in a broad range of industrial applications, such as drag reduction on an airplane wing, or the cooling of micro-components in a micro-electromechanical system (MEMS). Other SJ applications include separation control, mixing enhancement and thrust vectoring.

1.2 Synthetic Jet Ejector (SJE)

A jet ejector includes a primary jet of fluid, which entrains additional secondary flow from the surroundings and discharges a mixture of primary jet and entrained fluid from the end of a mixing tube [12]. In the case of a synthetic jet ejector, the primary jet is a synthetic jet. One configuration is shown in Figure 1.2. In this device a SJA produces a SJ, which creates a suction pressure around the annular space between the

actuator and the shroud. During the cycle, air is introduced into the mixing area because of the pressure difference. The mixture is then discharged at the other end of the shroud.

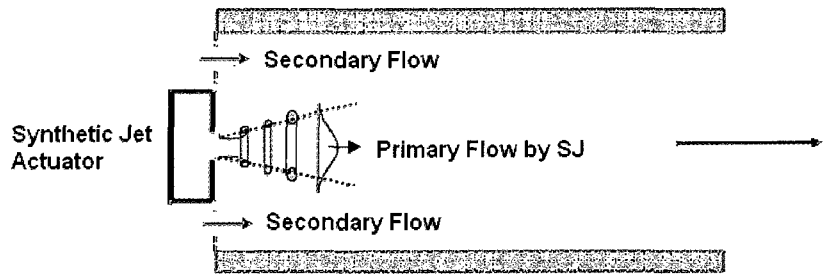

Figure 1.2 Schematic of SJE.

Certain configurations of these devices have been shown to be effective in cooling electronic equipment [10].

1.3 Objectives

This thesis contains a numerical investigation of a particular synthetic jet ejector configuration, which may have application to automotive seat ventilation. Of particular interest are the following objectives:

- To determine the optimum geometrical and operating parameters for the selected SJE configuration.
    - Develop a numerical finite volume solution methodology.
    - Determine suitable grid size and time step size for efficient calculations.
    - Use the efficient numerical model to conduct a parametric study.
    - Identify the best values for parameters for optimum flow rate.
- To investigate dimensionless parameters for representing synthetic jet ejector data.

- To determine the feasibility of an automotive seat ventilation application.

1.4 Scope

Chapter 2 starts with a discussion of dimensionless groups, followed by a review of the literature that is pertinent to this study. Chapter 3 includes a description of the numerical model of the synthetic jet ejector. Also included in Chapter 3 are some preliminary studies to determine an efficient numerical model. The numerical experiments that were conducted to determine the optimum geometry and operating conditions are presented in Chapter 4. A discussion of the application of the results to the automotive seat ventilation problem is presented in Chapter 5. Conclusions and recommendations are given in Chapter 6.

CHAPTER 2

DIMENSIONLESS GROUPS AND LITERATURE SURVEY

In order to make the material easier to understand, this chapter begins with a summary of the common dimensionless groups used to describe synthetic jets, as well as some of the characteristic features of these jets. This is followed by the SJE geometric variables and flow rate equations. The last section is devoted to a discussion of some of the pertinent previous numerical studies that have been reported in the literature.

2.1 Common Dimensionless Groups

One of the most important dimensionless numbers in viscous fluid flow is Reynolds number, *Re*. For a steady jet, the Reynolds number is defined as,

$$Re = \frac{Vd}{\upsilon} \tag{2.1}$$

where V = area-average velocity at the exit

d = orifice diameter

υ = kinematic viscosity

As mentioned in Chapter 1, the synthetic jet is an unsteady jet, so a time mean value of velocity is needed for its Reynolds number calculation. However the time mean value of the area-averaged velocity at the exit is zero, because the SJ has a zero net mass flux and therefore cannot be used as a velocity scale. In order to facilitate a comparison between a synthetic jet and a steady jet, Smith and Glezer [21] proposed the use of the velocity scale

$$U_0 = f L_0 = \frac{1}{T}\int_0^{T/2} V_p(t)dt \tag{2.2}$$

where $V_p(t)$ = orifice area-average velocity as a function of time

T = actuator diaphragm vibration period

$f = \frac{1}{T}$, actuator driving frequency

$L_0 = \int_0^{T/2} V_p(t)dt$, stroke length

The stroke length can be interpreted as the length of a slug of fluid (air) pushed from the orifice during the ejection phase, as shown in Figure 2.1.

U_0 is the downstream-directed velocity, which occurs only during the ejection half of the cycle, averaged over the full cycle [20]. For a sinusoidal velocity variation, $V_p(t) = V_A \sin(2\pi f t)$, where V_A is the inlet velocity amplitude, and the stroke length can be evaluated to give

$$L_0 = \frac{V_A}{\pi f} \tag{2.3}$$

and the velocity scale is

$$U_o = \frac{V_A}{\pi} \tag{2.4}$$

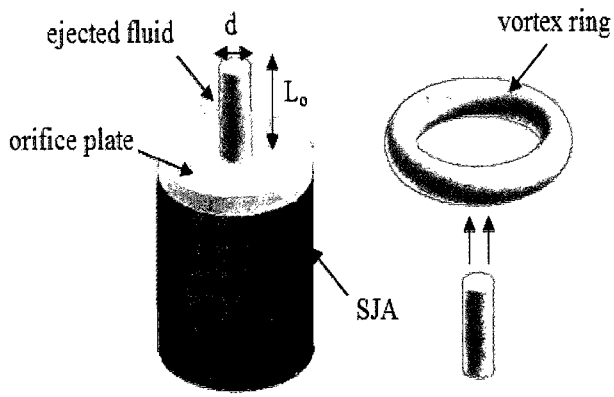

Figure 2.1 Schematic of stroke length and vortex ring.

Based on this velocity scale defined by (2.2), the Reynolds number for a synthetic jet is given by

$$Re_{U_0} = \frac{U_o d}{\upsilon} \tag{2.5}$$

For unsteady flow with a characteristic frequency of oscillation, the Strouhal number is also a very important dimensionless group. In terms of the velocity scale defined above, the Strouhal number is given by

$$St = f\frac{d}{U_o} \tag{2.6}$$

or in the case of sinusoidal input

$$St = f\frac{d\pi}{V_A} \tag{2.7}$$

The product of Reynolds number and Strouhal number is $\frac{fd^2}{\upsilon}$, which is the square of the Stokes number, S, or

$$S = \sqrt{\frac{fd^2}{\upsilon}} \tag{2.8}$$

The Reynolds number and Strouhal number for a synthetic jet ejector are defined in Appendix A.

For the steady jet, the region near the nozzle exit and along the central portion is called the potential core. This region has the characteristic of having a constant velocity and is surrounded by the shear layer. A shear layer is a region where the velocities of adjacent fluid layers are different. This region is highly unstable and leads to the generation of strong turbulent fluctuations and the entrainment of surrounding fluid into the jet. The shear layers merge toward the centre of the jet as the distance from the nozzle exit increases and the potential core eventually disappears. Downstream of the potential core, the centreline mean velocity decreases [18]. In contrast, the centreline velocity of a synthetic jet starts with a zero value at the nozzle exit, and rises to a maximum before decaying according to the -1/2 power-law typical of plane jets [20] as shown in Figure 2.2.

The width of a jet usually refers to the cross-stream radius at which the streamwise velocity is half of the centreline value. The width of both the steady jet and synthetic jet grow linearly in the downstream direction. In the near field, SJs grow more rapidly in the flow direction, both in terms of jet width and volume flux, than do steady jets with the same Reynolds number. That is because SJs are dominated by vortices that entrain more fluid than do steady jets. In the far field, SJs resemble steady jets in that the self-similar velocity profiles are identical [20]. In this region, it appears that SJs behave just like steady jets.

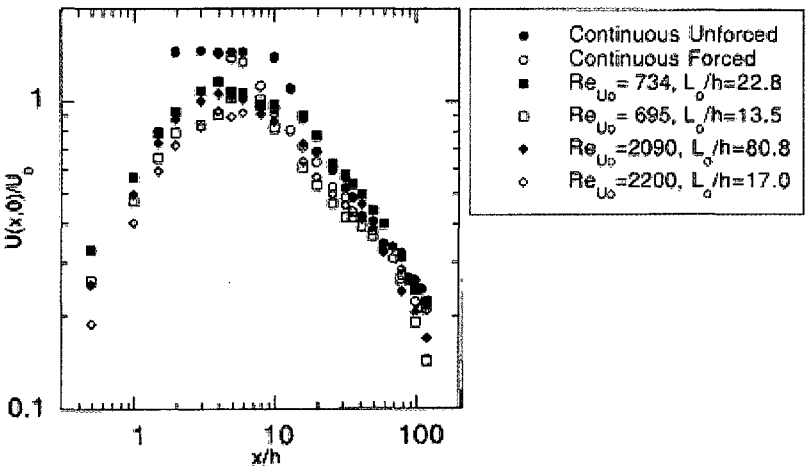

Figure 2.2 Time-averaged centreline velocity versus downstream distance. h refers to the actuator exit width [20].

Another characteristic of jets is entrainment, which is the ability to draw in surrounding fluid. The entrainment coefficient is given by [26]

$$C_e = \frac{d}{M_j}\left(\frac{\rho_j}{\rho_s}\right)^{1/2}\frac{\Delta \dot{M}_e}{\Delta x} \tag{2.9}$$

where $\dot{M}_j$ =jet mass flow rate at the orifice

ρ_j =jet density at the orifice

ρ_s = density of surrounding atmosphere

$\dot{M}_e$ = entrained mass flow rate up to position x

x = axial distance from orifice exit plane

The ratio $\Delta \dot{M}_e / \Delta x$ is also referred to as the entrainment rate. It was first measured by Ricou and Spalding [16] for a fully developed steady turbulent axisymmetric free gaseous jet. Hill [5] extended Ricou and Spalding's work to measure directly the local entrainment rate in the initial region of axisymmetric turbulent air jets. These experimental results showed that the entrainment coefficient, C_e, increases non-linearly from 0.11 at one diameter downstream of the jet nozzle orifice to a fully

developed value of 0.32 at about 13 diameters downstream. When acoustically pulsed, the entrainment coefficient increased to 4.5 times greater at x/d=10 and to 5.2 times greater at x/d=17.5 [26]. For synthetic jets, $\dot{M}_j$ is zero, and $\dot{M}_e$ reaches a constant value when the system has achieved time-periodic state. Hence the entrainment coefficient or entrainment rate definitions do not apply and must be modified.

2.2 Synthetic Jet Ejector Operation

The geometry of a typical two-dimensional synthetic jet ejector is shown in Figure 2.3. The synthetic jet actuator diameter is D, and the exit orifice diameter is d. The diameter for the mixing tube or shroud is denoted by D_e. D and d can be varied to obtain different flows. The centreline, or the symmetry line, for this flow is parallel to the x axis and passes through the origin. The oscillating primary flow induces a secondary flow which travels through the device. Although the time average of the primary flow at the actuator exit is zero, that of the secondary flow and hence the total flow is non-zero.

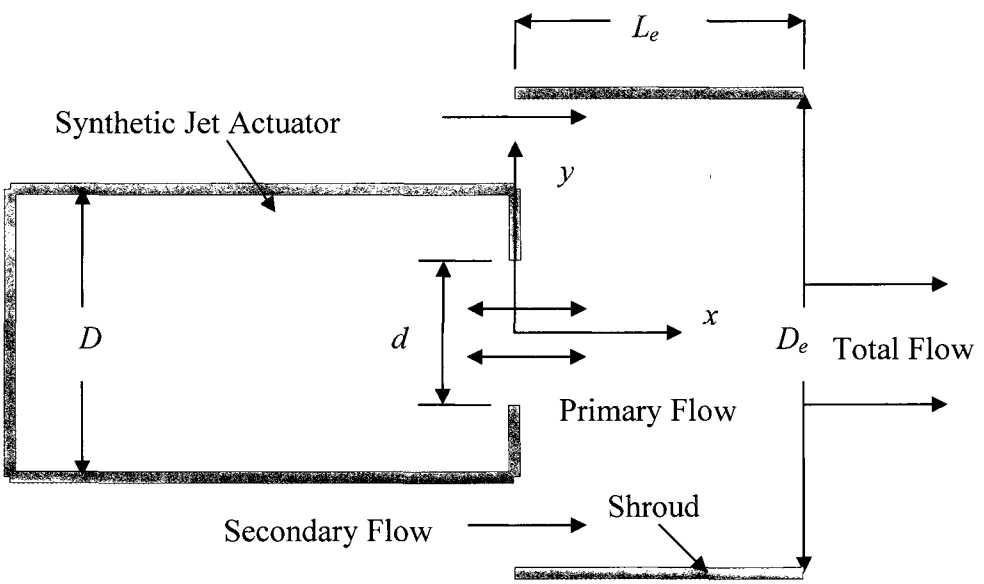

Figure 2.3 Geometric definitions of SJE.

2.3 Time-averaged Quantities

For any time periodic flow the concept of a time-averaged quantity is necessary to determine the net effect over a complete cycle. Any period averaged quantity is defined as the time integral of the value over one period, T, divided by the period. These period averaged quantities are denoted by the variable with a bar over the top. For example, the period area-averaged secondary flow velocity, $\overline{U}_s$, is defined as

$$\overline{U}_s = \frac{1}{T}\int_t^{T+t} V_s(t)dt \tag{2.10}$$

where time is denoted by t and V_s is the area-averaged secondary flow velocity.

When the number of time steps per cycle, $n = \frac{T}{\Delta t}$, the variable, say $V_s(t)$ in this case, will be calculated for each time step, then $\overline{U}_s$ can be approximated as the average of the sum over one cycle, or

$$\overline{U}_s = \frac{\sum_{k=1}^{n} V_{s,k}}{n} \tag{2.11}$$

where subscript k is an integer between 1 and n which indicates evaluation at the kth time.

The flow is said to have reached a time periodic state when the time-averaged flow becomes independent of the number of periods that have passed. In reality, the ideal time periodic state is asymptotically reached. It is one of the objectives of this project to determine an acceptable condition when the time periodic state has been reached. Many variables can be chosen to use to decide when the time periodic state has been reached. Because we are only focusing on the SJE ventilation effects, the period area-averaged secondary inlet velocity is chosen in this study. The criterion for time periodic state used in this thesis is when the period area-averaged secondary inlet velocity difference between consecutive cycles is less than 0.1% or $1.0\text{x}10^{-3}$ m/s, whichever comes first.

2.4 Volume Flow Rate

In this study, interest focuses on two volume flow rates, the inlet flow rate and the outlet flow rate. The inlet flow consists of the primary flow and the secondary flow as shown in Figure 2.3. The outlet flow is the mixture of the two inlets, however, the period area-averaged value of the primary flow is zero $\left(\overline{U}_p = 0\right)$, and hence the period area-averaged secondary inlet and outlet flows are equal. Period area-averaged velocity will be used to calculate the volume flow rate. The volume flow rates are given by,

$$\dot{Q}_{primary} = \dot{Q}_P = \overline{U}_p \times A_p = 0 \tag{2.12}$$

$$\dot{Q}_{secondary} = \dot{Q}_s = \overline{U}_s \times A_s \tag{2.13}$$

$$\dot{Q}_{inlet} = \dot{Q}_i = \dot{Q}_p + \dot{Q}_s = \dot{Q}_s \tag{2.14}$$

$$\dot{Q}_{outlet} = \dot{Q}_o = \overline{U}_t \times A_t \tag{2.15}$$

2.5 Pertinent Numerical Studies

Over the years, a considerable amount of research has been done on the numerical simulation of synthetic jets. These are reviewed below along with selected studies from the closely related field of pulsating jets.

Kral et al. [7] performed two-dimensional incompressible simulations of a synthetic jet with a quiescent external flow. The computational domain encompassed only the region external to the jet without the cavity or actuating membrane. In place of an actuator, a sinusoidal velocity profile was prescribed as a boundary condition at the jet exit. This avoided the flow calculations within the cavity. Both laminar as well as turbulent jets were studied. They found that the laminar jet did not capture the breakdown of the vortex train that was observed experimentally. It was also noticed that the jet produced a non-zero mean streamwise velocity even though it operated with zero net mass flux at the nozzle exit.

Rizzetta et al. [17] performed a numerical study, using Direct Numerical Simulation (DNS) to solve the unsteady compressible Navier Stokes equations for both the interior of the actuator cavity and for the external jet flow field. An oscillatory displacement boundary condition was prescribed at the lower end of the cavity. They showed that the internal cavity flow becomes periodic after several cycles. Therefore, it was considered appropriate to use the periodic velocity profile at the slit plane as a boundary condition in subsequent runs involving the external domain only. This effectively caused the cavity flow to decouple from the exterior flow. It was observed that the planar 2-D simulations could not capture the breakdown of the vortices as a result of the spanwise instabilities. They suggested that a 3-D simulation would be a more proper approach for the planar opening.

Lee and Goldstein [8] used the DNS method developed by Kral et al [7] to study the effects of fluid and geometric parameters on the resulting flow field in two-dimensional synthetic slot jets pulsing into initially quiescent flow. The jet evolution was found to depend strongly on the Strouhal number. Their results indicated that the shape of the lip and depth of the cavity were important parameters in the resulting flow. A thicker orifice lip would lead to a more uniform velocity profile at the orifice and an increase in the rate of the formation of vortices. Compared with the round orifice lip, a straight orifice lip changed the orifice velocity profile, but there was no subsequent change in either the formation of vortices or the synthetic jet flow.

Fugal [3] also used DNS to study how the exit geometry and dimensionless stroke length change the synthetic jet characteristics formed by a fully developed oscillating channel flow. It was observed that the $k-\varepsilon$ turbulence model more accurately predicts the downstream behavior of the jet. He found that the magnitude of the stroke length required to form a jet increases as the exit radius increases. He also performed a detailed grid size and temporal resolution study for the synthetic jet CFD solution.

Mallinson et al. [11] investigated the synthetic jet flow both experimentally and computationally. They used a commercial Navier-Stokes solver called CFX4.2 for the unsteady incompressible numerical simulations. The $k-\varepsilon$ model was chosen as the turbulence model. The experimental data and computational results for centreline and

profile velocity distributions are in good agreement with each other. They found that the maximum velocity for a particular actuator configuration seemed to depend on a balance between inertia (diaphragm forcing) and viscous (orifice boundary layer) forces.

Rampunggoon [14] numerically investigated the dynamics of synthetic jets in the presence of cross-flow as well as jets issuing into quiescent air using an incompressible Navier-Stokes solver in a two-dimensional configuration. A comprehensive parametric study was carried out where the diaphragm amplitude, external flow Reynolds number, boundary layer thickness, and slot dimensions were varied and scaling of the jet characteristics with various parameters examined. It was shown that large mean recirculation bubbles are formed in the external boundary layer only if the jet velocity is significantly higher than the cross-flow velocity.

Utturkar et al. [23, 24] performed two-dimensional numerical simulations to study the sensitivity of synthetic jets to the design of the jet cavity. They considered the placement of the oscillating diaphragms as well as changes in the cavity aspect ratio. Both quiescent and external cross-flow have been investigated. The authors also proposed and validated a jet formation criterion $\frac{Re_{U_o}}{S^2} > 2$ and $\frac{Re_{U_o}}{S^2} > 0.16$ for two-dimensional and axisymmetric synthetic jets, respectively.

Ravi et al. [15] conducted a three-dimensional numerical simulation to study the formation and evolution of large aspect ratio synthetic jets issuing into quiescent air. They used a finite difference based Cartesian grid immersed boundary solver, which is capable of simulating flows with complex 3-D, stationary and moving boundaries. It was found that the vortex train emanating from the nozzle exit undergoes axis-switching and assumes a complex shape. From the mean structure of the jet, they concluded that the jet spreading would be helpful in entrainment of the ambient fluid.

Not many numerical studies have been completed for synthetic jet ejectors. Vermeulen et al. [27] conducted both a CFD analysis and experiments to show that adding a pulsation to a steady primary jet flow improves ejector performance. They also showed that a strong synthetic jet actuator gives ejector performance as good as a pulsed

primary flow jet. The pumping effectiveness, defined as the mass flow rate ratio $\frac{M_s}{M_p}$, increased by up to 4.5 times that for a steady jet. Their CFD study, however, did not contain either a grid convergence or a time step convergence study.

CHAPTER 3

EFFICIENT SYNTHETIC JET EJECTOR NUMERICAL MODEL

This chapter presents details of the computational model developed to conduct the numerical experiments involving SJEs. It includes a description of the computational domain used for the SJE simulation, followed by the boundary conditions of the model. In order to create the most efficient model to use in the numerical experiments, grid convergence, grid structure and time step size studies are conducted.

All simulations use the $k-\varepsilon$ turbulence model (validated in Appendix B) along with the second-order upwind scheme for spatial discretization and second-order implicit scheme for time advancement. The commercial CFD package, FLUENT 6.3, is used to solve the flow field equations. More details about the setup can be found in Appendix C.

The results of a preliminary parametric study is also included to determine the trends in the variation of output flow rate and pressure difference with orifice diameter, actuator diameter, shroud diameter, shroud length and primary inlet velocity amplitude.

The computer used in this study has a P5K-E ASUS Motherboard with an Intel Corel 2 Quad Q6600 Central Processing Unit (CPU) running at 2.4 GHz with 8 GB of DDR2 1066 MHz Ram. A 64-bit Windows XP Professional operating system is used.

3.1 Computational Domain

Figure 3.1 is a 3-D schematic representation of the SJE domain. Because the SJE is axisymmetric in this study, a 2-D axially symmetric simulation is sufficient. The SJA will be excluded from the computational domain since the assumption of a top-hat velocity profile at the orifice exit combined with a sinusoidal time variation is a good approximation for simulating the exit flow [17]. Therefore, the calculation domain consists of the gridded area shown in Figure 3.2.

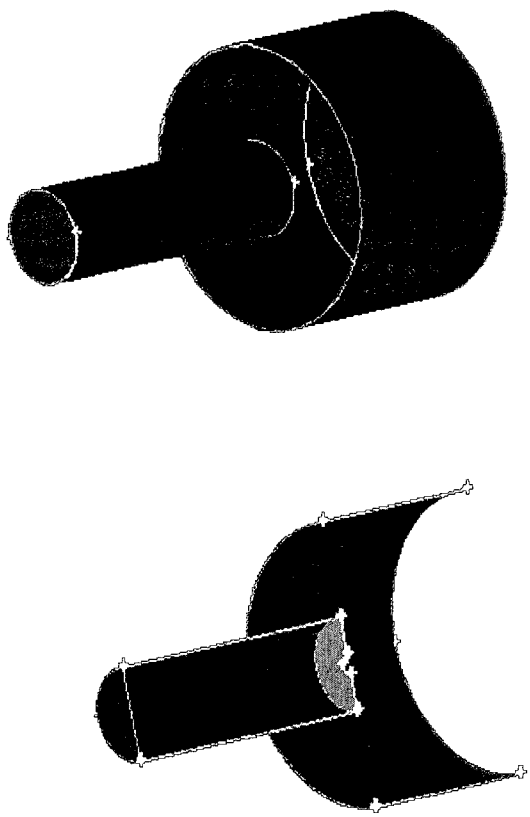

Figure 3.1 3-D schematic representation of SJE.

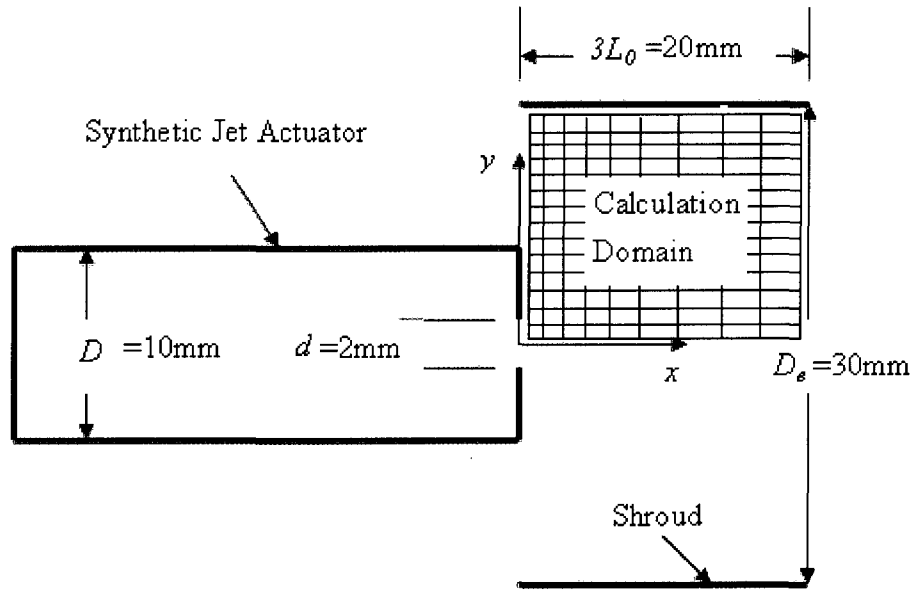

Figure 3.2 Geometric diagram of initial SJE domain.

The extent of the mixing length for a SJ is determined from the stroke length. Fugal [3] found that the extent of the computational domain is sufficient at three stroke lengths, $3L_0$, in his study of SJ flow. Therefore $3L_0$ will be the shortest length taken for the SJE's in this study. According to Equation (2.3), $L_0 = 6.59\times10^{-3} m$, therefore, $3L_o \approx 20\ mm$. The initial values of the SJE geometrical and operating parameters used in the initial simulation are summarized in Table 3.1.

Table 3.1 SJE initial geometrical and operating parameters.

SJE Parameters	Values
SJA orifice diameter, d (m)	0.002
SJA cavity diameter, D (m)	0.01
SJE shroud diameter, D_e (m)	0.03
SJE shroud length, L_e (m)	0.02
Input frequency, f (Hz)	1,450
Air density at 25^0C, ρ (kg/m^3)	1.19
Air dynamic viscosity at 25^0C, μ (N s/m^2)	1.84e-5
Primary inlet velocity amplitude, V_A (m/s)	30

3.2 Boundary Conditions

The boundary conditions used for the SJE simulations are shown in Figure 3.3. The right side is the exit of the SJE which is open to the atmosphere and hence has a zero gauge pressure. The bottom is the centreline, so it is modeled as an axis because of axisymmetry. The primary inlet flow, which is the SJA outflow, is specified using a sinusoidal function, $V_p(t) = V_A \sin(2\pi f t)$. The SJA orifice plate and the mixing tube wall are modeled as no-slip walls. The opening for the secondary flow inlet, from where air is entrained into the mixing tube, is modeled as a pressure inlet. When this opening is open to the atmosphere, the pressure for this pressure inlet is zero gauge pressure. If the outside of this opening is attached to something, such as the form of the car seat, a negative gauge pressure is developed at this location, the value of which depends on the resistance that must be overcome for air to pass through. The effect of this resistance, or negative gauge pressure, on the total mixing flow rate, will be analyzed later in this study.

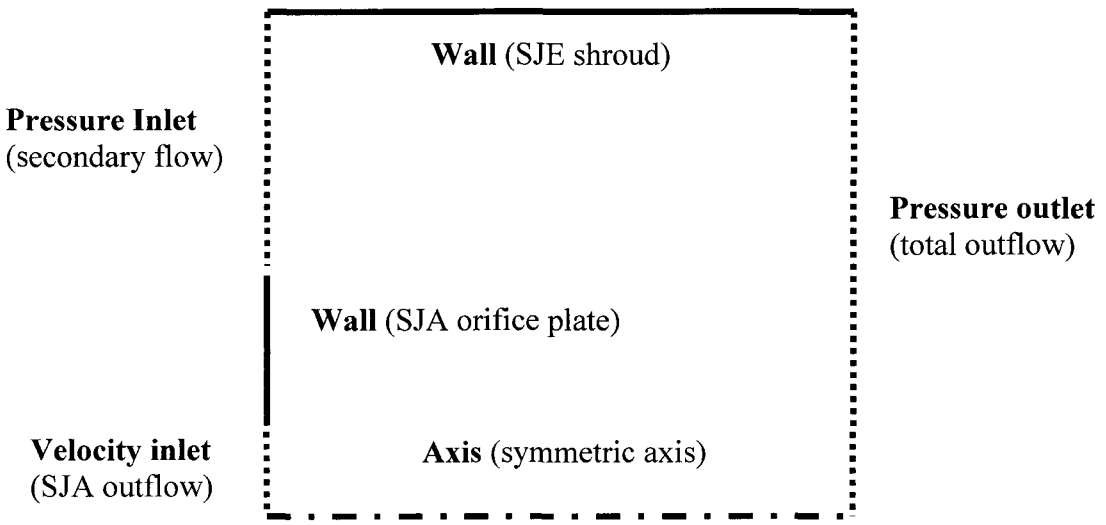

Figure 3. 3 SJE numerical model boundary conditions.

3.3 Grid Convergence Study

Numerical errors occur when the representation of the governing flow equations, which are continuous in time and space, are modeled as algebraic expressions in a discrete domain of space and time. This is referred to as discretization error. It is usually caused by an improper grid size or time step size. This section deals with the grid convergence, ie., when the solution no longer changes even when more grid points are added to the computational domain. Extra grid points waste computer CPU time and memory without achieving much additional accuracy.

Grid convergence is achieved by obtaining the solution for one case with a set number of grid points, then doubling the number of grid points and seeing how the quantities associated with the flow change. The process is repeated until no significant changes are observed with successive grid refinement. For engineering applications, a change within 10% is often considered to be acceptable. In this study, the results for many different cases are desired, hence it is impractical to perform a grid convergence study for each case. Thus, it is performed for one case and the results are generalized to the others.

In order to generalize the grid convergence results, Fugal [3] defines the concept of average cell area, A, which is the total area of the computational domain divided by the total number of cells in the simulation model. By applying this concept to SJE flow, the quantity A is then made non-dimensional using D_e^2 to produce a dimensionless average cell area, A', which scales with the extent of the computational domain. A larger computational domain then requires more cells to have the same average cell area as a smaller domain. With this concept, a grid convergence study conducted on one case can be used to generalize the results to other cases by keeping the dimensionless average cell area constant.

The original case selected to determine the optimum grid resolution has the settings shown in Table 3.1, i.e.,

$$3L_0 = 20 \ mm$$
$$D_e = 30 \ mm$$
$$Number\ of\ cells = 400 \times 120$$
$$A' = \frac{A}{D_e^2} = \frac{3L_0 \times 0.5D_e \Big/ Number\ of\ cells}{D_e^2} = \frac{(20 \times 15)/(400 \times 120)}{30^2} = 6.94e-6$$

In order to compare the effects of grid resolutions, the period area-averaged secondary inlet velocity $\overline{U}_s$, is selected as the variable for comparison. It is calculated for six different grid resolutions, corresponding to A' values of 4.44e-4, 2.22e-4, 1.11e-4, 5.56e-5, 2.78e-5 and 6.94e-6. The results are then cast in the form of a percent difference, calculated as the absolute per cent difference between the given solution and the finest solution divided by the finest solution, as shown in Equation (3.1).

$$\%\ Difference = \frac{\left| \overline{U}_{s,A'} - \overline{U}_{s,A'=6.94e-6} \right|}{\overline{U}_{s,A'=6.94e-6}} \times 100 \qquad (3.1)$$

As mentioned in section 2.3, $\overline{U}_s$ is calculated after the time periodic state is reached. By applying the criterion for time periodic state, the original case reaches the time periodic state condition after 24,400 time steps (61 cycles) as shown in Figure 3.4.

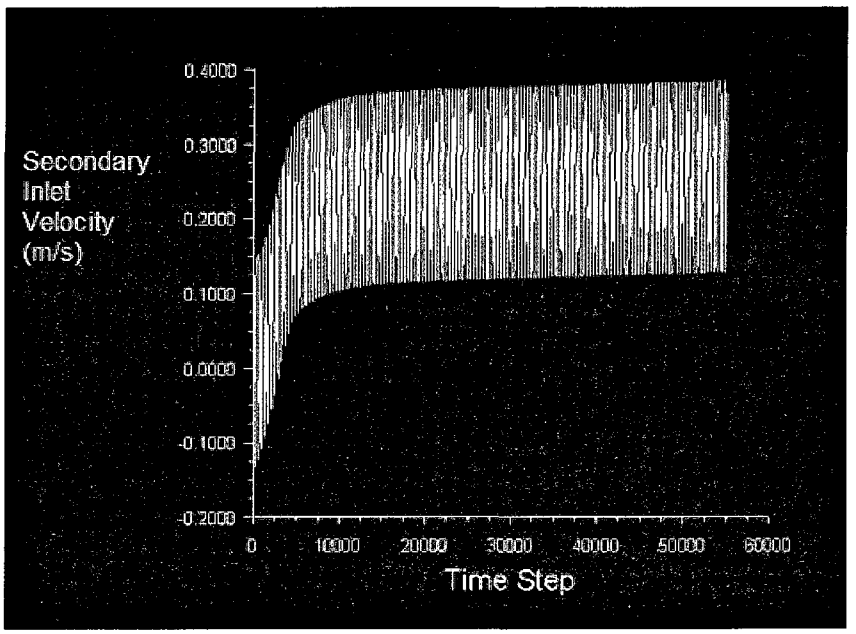

Figure 3. 4 Time history for area-averaged secondary inlet velocity for original case, 400 time steps per cycle.

The value of $\overline{U}_s$ is 0.277 m/s after 61 cycles, and increases to 0.300 m/s after 350 cycles. The difference is 7.57%, which is less than 10%, and hence considered acceptable. Using 0.1% as the cut-off criterion is therefore considered valid. The grid resolution study results are summarized in Table 3.2. This table gives the cut-off cycle numbers, computer CPU time per cycle, total CPU time to cut-off, $\overline{U}_s$ and the percentage difference in $\overline{U}_s$ relative to the base for the various A' values. As the A' value gets larger, less grid points are used in the same domain, and it takes less CPU time to finish one cycle because of the smaller number of calculations.

Table 3.2 Grid resolution study.

Grid Resolution, Dimensionless Average Cell Area (A')	**Cut-off Cycle Number (0.1% criteria)**	**Computer CPU Time per Cycle (mins.)**	**Total CPU Time to Cut-off (mins.)**	**Period Area-Averaged Secondary Inlet Velocity, $\overline{U}_s$ (m/s)**	**% Difference in $\overline{U}_s$ (Equation (3.1))**
4.44e-4 (1/64th)	59	3-4	207	0.288	3.82%
2.22e-4 (1/32nd)	49	3-4	172	0.284	2.34%
1.11e-4 (1/16th)	**42**	**5-6**	**231**	**0.274**	**1.08%**
5.56e-5 (1/8th)	41	5-6	226	0.276	0.577%
2.78e-5 (1/4th)	46	8-9	391	0.278	0.072%
6.94e-6 (1/1)	61	27-30	1,740	0.277	N/A (Base)

It is evident that the percent difference in $\overline{U}_s$ is under 2% for A'=1.11e-4. From an engineering design point of view, this difference is quite acceptable. It is also important to note that there is approximately seven times reduction in computational time to reach time periodic state compared to the finest grid case. Although the A'=5.56e-5 case has approximately the same performance, the A'=1.11e-4 is chosen based on the general feeling that fewer cell numbers result in lower computational time for other cases.

3.4 Grid Structure Similarity

As mentioned in the previous section, the more grid points used, the more accurate the numerical solution will be. The grid point distribution is also important. Usually, more grid points are clustered in regions where high gradients are expected and less grid points are used in regions where gradients are low. Improper grid point distribution in the calculation domain might result in more computational time to converge or give poor results. In this study, the region near the inlets has large gradients because of the oscillating flow of the primary inlet and the swirling of the vortices across the secondary inlet surface. The shape of the calculation domain is rectangular. A structured grid with clustered grid lines near the inlet region was created using the commercial package, Gambit. During the course of this study, it is necessary to change the geometry in order to determine the optimum values for some parameters, such as the shroud diameter, D_e, or shroud length, L_e. This leads to a change of the calculation domain dimensions and grid structure. For the same calculation domain, even with the same number of cells (same A' value), a change in the grid structure can have an effect on the solution. In order to prevent this from influencing the trend of the results, the calculation domain grid structure is kept similar for all simulations.

As shown in Figure 3.5, the grid lines are clustered near the inlets in the x direction but spaced uniformly in the y direction. The aspect ratio for this 2-D grid structure is the ratio of the length of the long side of the cell to the short side of the cell, $\Delta x / \Delta y$. An Excel spreadsheet was created to calculate the aspect ratio of the first column of cells adjacent to the inlets and orifice plate, so that its value can be maintained at a value of one (1). The filename of the Excel file is aspectratio.xls and is included on the data CD accompanying this thesis. The following equations are used to determine the aspect ratio, $\Delta x / \Delta y$.

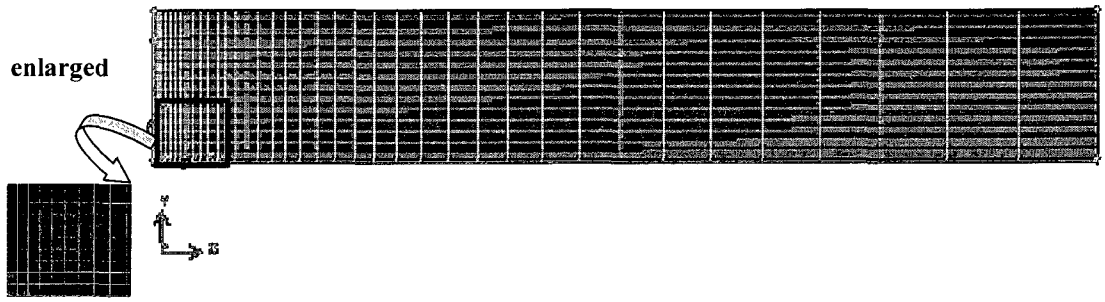

Figure 3.5 Calculation domain with uniformly spaced grid lines in *y* direction but clustered near inlets in *x* direction.

$$\Delta x = \frac{W f_a^{N-1}(1 - f_a)}{1 - f_a^N} \tag{3.2}$$

$$\Delta y = \frac{H}{M} \tag{3.3}$$

$$\text{First Column Aspect Ratio} = \Delta x / \Delta y \approx 1.0 \tag{3.4}$$

where W = extent of the calculation domain in the x direction

f_a = cluster factor in the range of 0 to 1

N = number of cells along x axis

M = number of cells along y axis

H = extent of the calculation domain in y direction

When the dimensions of the calculation domain are known, the number of grid points both on the x axis and y axis are specified. By trial and error, the value of f_a is chosen such that the aspect ratio is as close to 1.0 as possible.

Simulation results with grid structure as prescribed above seem to converge well and have been shown to give very consistent results.

3.5 Time Step Size Study

A second-order implicit time discretization scheme, commonly accepted as more accurate than the first-order, is used to approximate the time dependence of the solution. Caution must be taken to examine the sensitivity of the simulation results to changes in the magnitude of the time step size. Improper time step size will either cause the solution to be more unstable or give poor results. As with the grid size, the required time step size must be determined by comparing results for successively smaller/larger time step sizes. Starting with the model for an A' value of 1.11e-4, the first time step size is determined by dividing the period into 400 steps giving a period area-averaged secondary inlet velocity $\overline{U}_s$ of 0.274 m/s, which is taken as the base value. When another time step size with 500 time steps per cycle (TSPC) is used for comparison, using Equation (3.1), the difference is only 0.110%. Table 3.3 gives the $\overline{U}_s$ and percentage difference from the base case for a number of different TSPC and Δt values. TSPC values of 25, 50, 100, 200, 400 and 500 were selected and the respective $\overline{U}_s$ compared with the base value of the 400 TSPC using Equation (3.1).

Table 3.3 Time step size study results.

Time Steps per Cycle (TSPC)	25	**50**	100	200	400	500
Period Area-Averaged S.I. Velocity, $\overline{U}_s$, (m/s)	0.289	**0.271**	0.271	0.273	0.274	0.275
% Difference with Base (Equation (3.1))	5.221	**1.301**	1.305	0.398	N/A (Base)	0.110
Time Step Size, Δt, (s)	2.76E-05	**1.38 E-05**	6.90E-06	3.45 E-06	1.72E-06	8.62E-07

For the case with a TSPC of 50, there is only 1.3% difference with respect to the base, and hence it is considered to be of sufficient accuracy for this study. The corresponding time step size of 1.38e-5 seconds is chosen as the largest one to use for any future calculations in this study.

As further evidence that this value is acceptable, a plot of the period area-averaged secondary inlet velocity history over one cycle is shown in Figure 3.6. The 50 TSPC and 400 TSPC lines are seen to overlay each other.

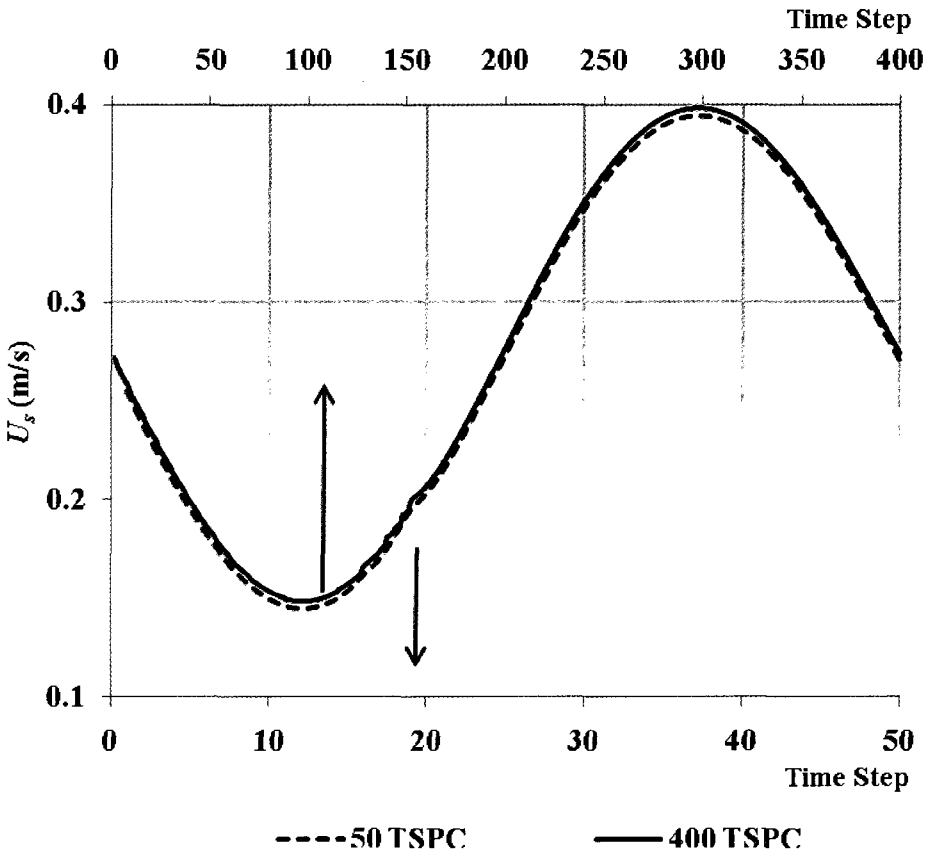

Figure 3.6 Period area-averaged secondary inlet velocity over one cycle with different time step sizes.

3.6 Preliminary Results

Using the geometry and numerical techniques outlined in the first five sections of this chapter, a series of numerical simulations using the efficient numerical model are conducted. The aim of these is to determine the trends in the variation of the SJE flow rate with changes in the various geometrical and flow parameters given in Table 3.1, along with the pressure difference between the secondary inlet and outlet.

Through dimensional analysis, detailed in Appendix A, the dimensionless flow rate is a function of the following dimensionless groups,

$$\frac{\dot{Q}_s}{D_e^2 V_A} = \phi\left(\frac{d}{D_e}, \frac{D}{D_e}, \frac{L_e}{D_e}, f\frac{D_e}{V_A}, \frac{\rho V_A D_e}{\mu}, \frac{\Delta p}{\rho V_A^2}\right) \qquad \text{(A10)}$$

The following preliminary results are obtained by changing one independent dimensionless group at a time while holding the others constant using the values found in Table 3.1. The density and viscosity values used are for air at standard atmospheric pressure (101,325 Pa) and a temperature of 25°C. In the cases where $\frac{\Delta p}{\rho V_A^2}$ is held constant, the secondary inlet and outlet are both assumed to be open to the atmosphere such that Δp is zero, which corresponds to the case of maximum flow.

3.6.1 Effect of Orifice Diameter

Orifice diameters of 2, 4, 6, 8, 9.9 and 10 mm are selected for study and the effect on dimensionless flow rate is plotted non-dimensionally in Figure 3.7. The trivial case of d=0 mm is also shown.

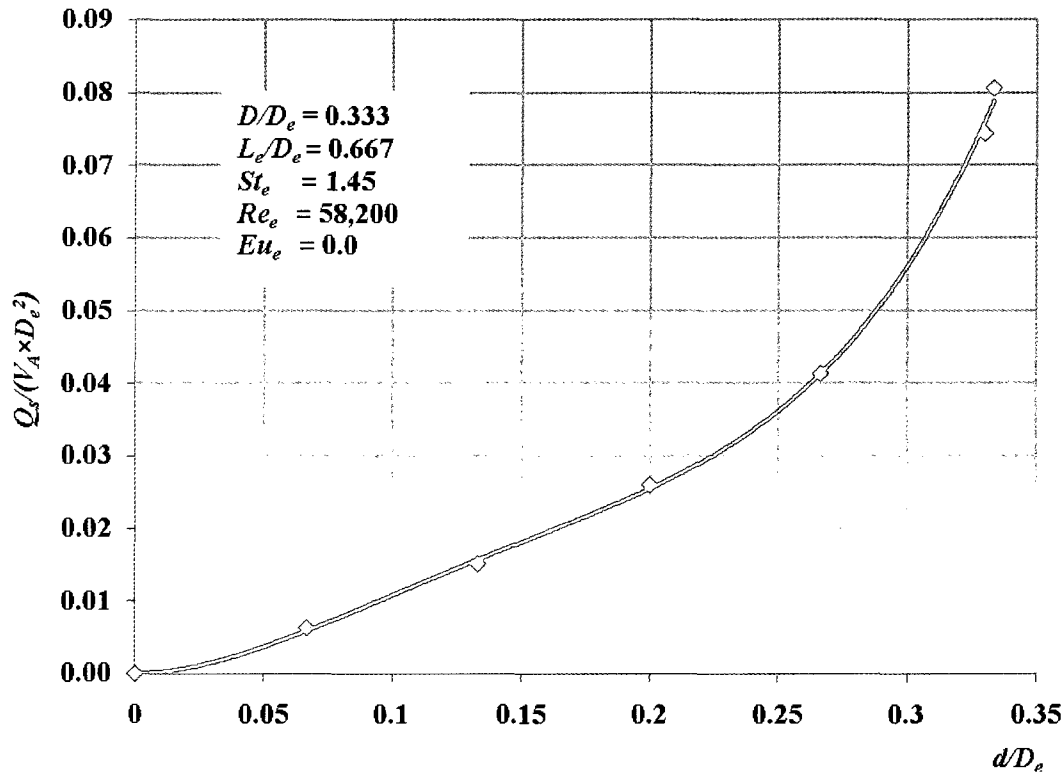

Figure 3.7 Effect of orifice diameter on dimensionless flow rate.

It can be seen that dimensionless flow rate increases as orifice diameter gets larger. Ideally, there will be no flow when the orifice diameter is close to zero, and the dimensionless flow rate has its highest value when the orifice diameter is the same as the actuator diameter. The question of whether the dimensionless flow rate goes up with larger actuator diameter, but fixed orifice diameter, will be explored in the next section.

3.6.2 Effect of Actuator Diameter

Actuator diameters of 2, 2.1, 5, 10 and 15 mm are selected for study and the effect on dimensionless flow rate is plotted in dimensionless form in Figure 3.8.

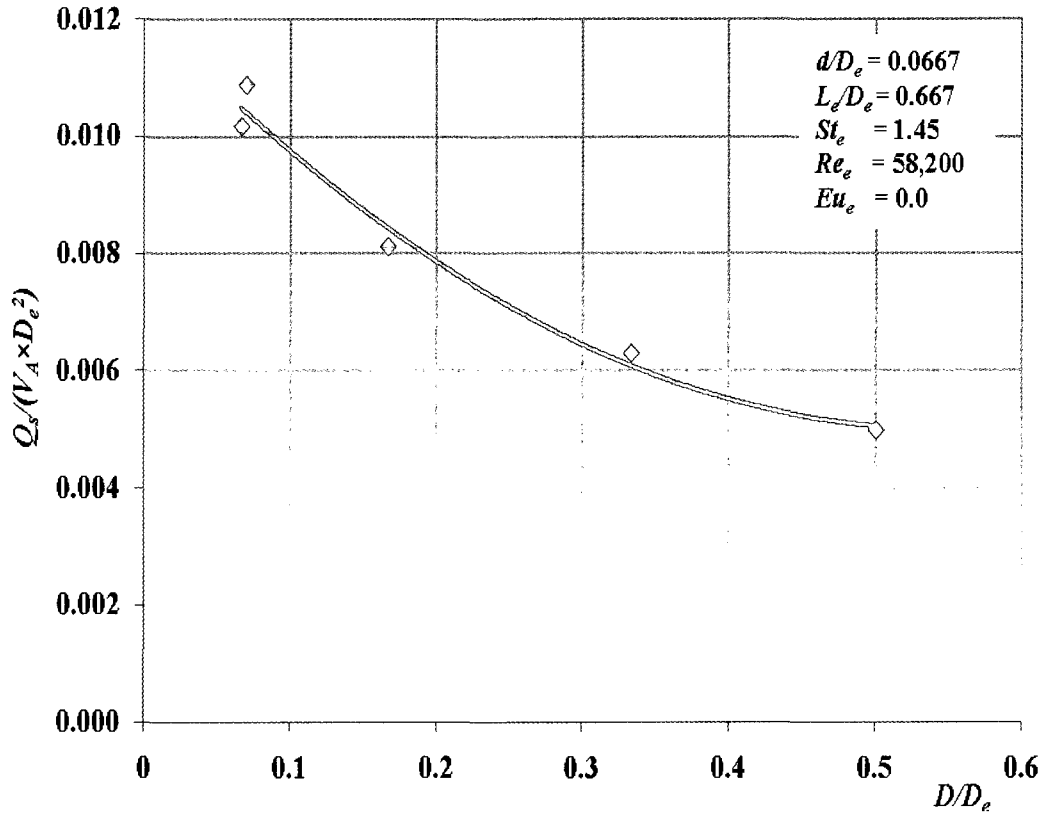

Figure 3.8 Effect of actuator diameter on dimensionless flow rate.

It is interesting to note that the dimensionless flow rate decreases as the actuator diameter becomes larger. This is because the secondary inlet area becomes smaller as the actuator diameter gets larger, and the entrainment effect caused by the primary flow also diminishes as the exit plate gets larger. This plot also confirms that the dimensionless flow rate reaches its maximum when the actuator diameter is close to the orifice diameter. This fact, coupled with that of the fact that flow rate increases with increasing orifice diameter implies that the orifice diameter should be as close to the actuator diameter as possible $(d \approx D)$.

3.6.3 Effect of Shroud Length

Shroud lengths of 20, 30, 40, 60, 80, 100, 130 and 160 mm are selected for study. The results are plotted non-dimensionally in Figure 3.9.

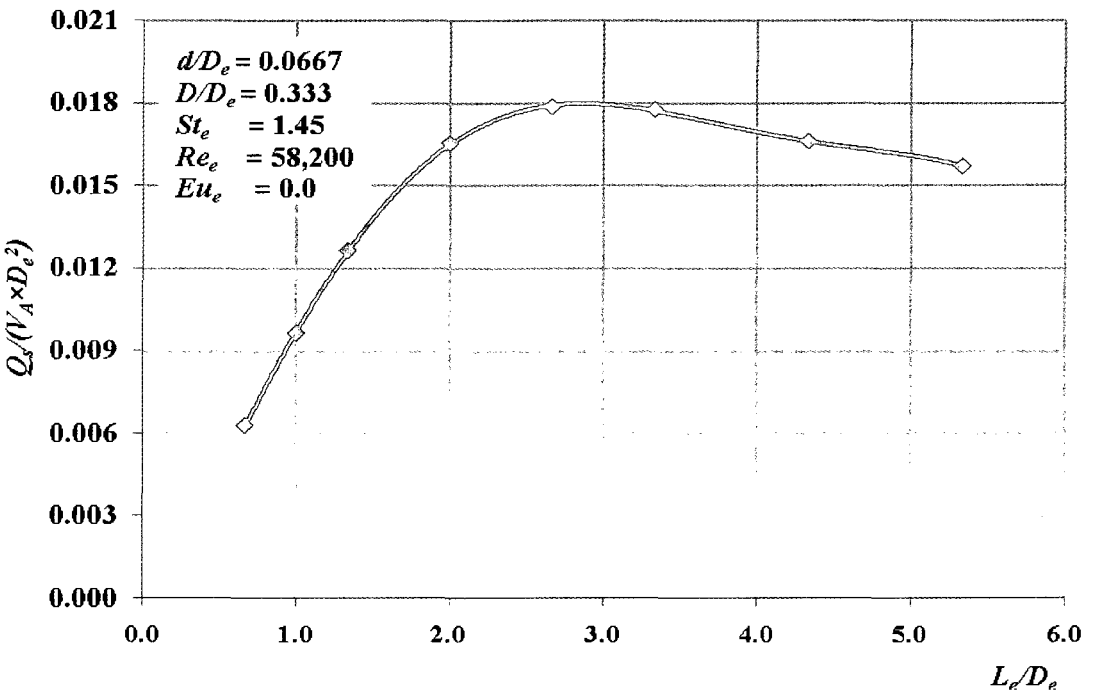

Figure 3.9 Effect of shroud length on dimensionless flow rate.

Dimensionless flow rate increases as shroud length increases. It reaches its peak then declines. This decline is due to the increase in flow resistance as the shroud length increases. This also implies that an optimum L_e/D_e exists.

3.6.4 Effect of Strouhal Number

Input driving frequencies of 250, 363, 725, 1,000, 1,450, 2,000, 3,000 and 4,000 Hz are chosen for study and the results are plotted in a dimensionless manner in Figure 3.10.

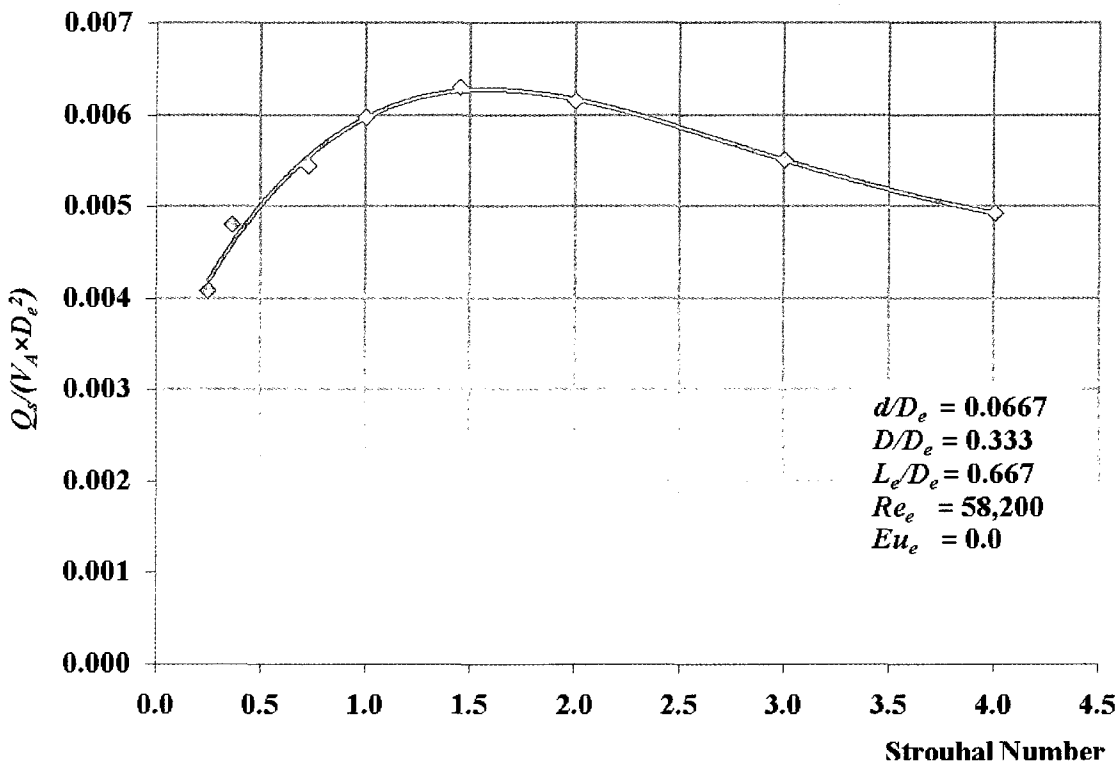

Figure 3.10 Effect of Strouhal number on dimensionless flow rate.

The trend is similar to the case of shroud length. The dimensionless flow rate increases rapidly with increasing Strouhal number. It reaches its peak at approximately 1.5 then flattens with higher Strouhal number. This may be a result of a resonance effect within the shroud.

3.6.5 Effect of Reynolds Number

Primary velocity amplitude values of 10, 20, 30, 40, 50 and 60 m/s are selected for study. The dimensionless results are presented in Figure 3.11. The trivial case of V_A=0 m/s is also shown.

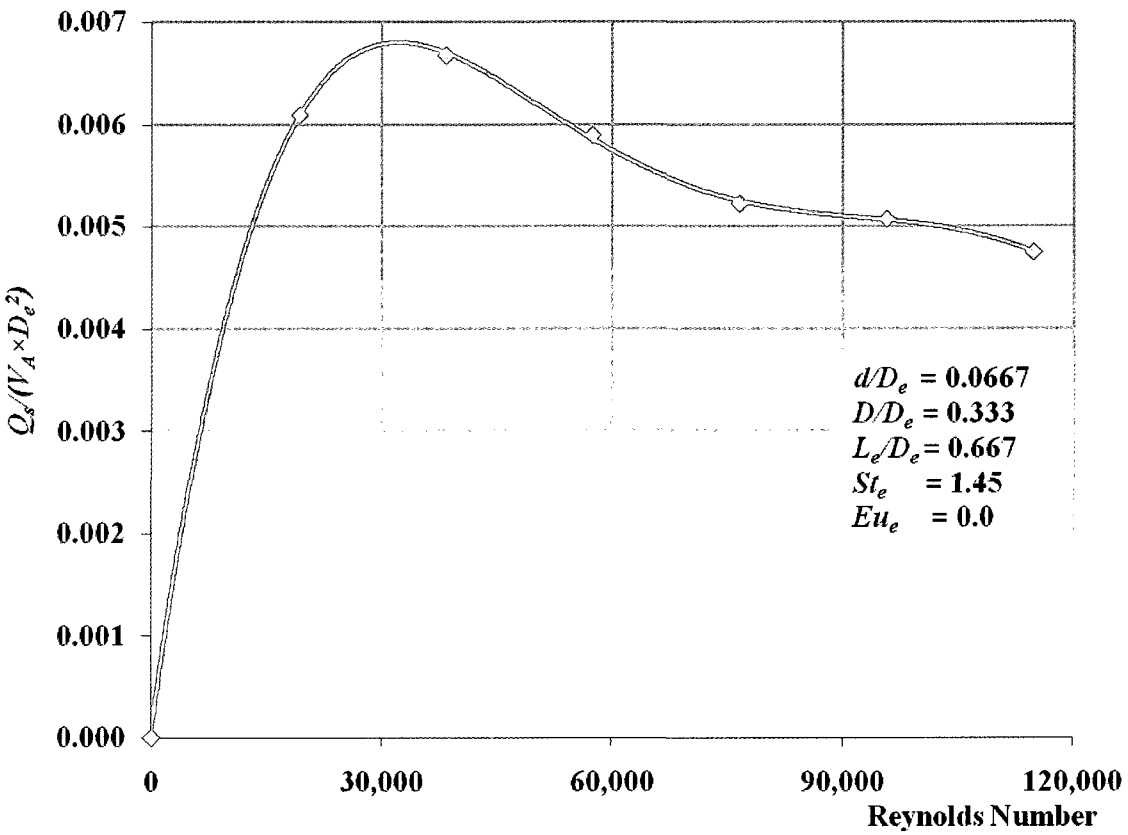

Figure 3.11 Effect of Reynolds number on dimensionless flow rate.

The dimensionless flow rate is very sensitive to the change of Reynolds number for low Re_e values. It reaches an optimum value at approximately 30,000 and then decreases. This indicates that an optimum operation will occur at a particular Re_e value with slightly decreased performance at higher values.

3.6.6 Effect of Euler Number

Various Euler numbers are selected for study and the flow rates plotted in dimensionless terms in Figure 3.13. The Δp value used is the output pressure minus the inlet pressure, which gives positive values.

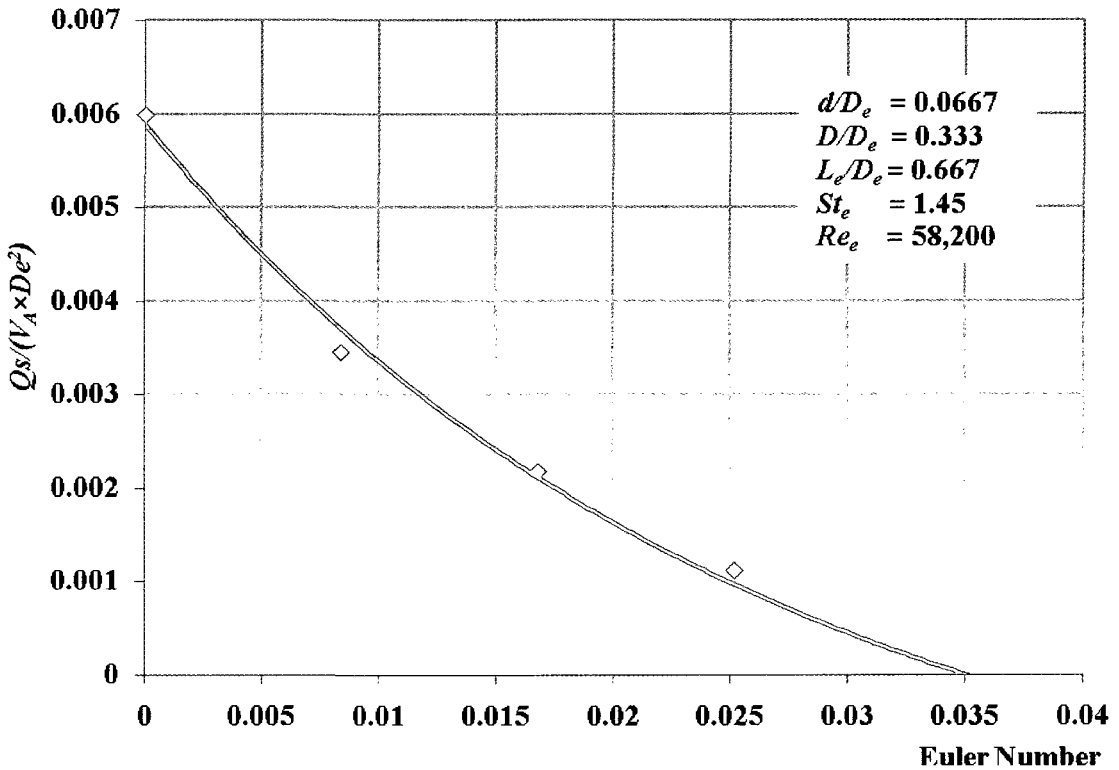

Figure 3.12 Effect of Euler number on dimensionless flow rate.

The dimensionless flow rate decreases with increasing Euler number. The maximum occurs when Euler number is zero, and decreases to zero when Euler number is at its maximum. This indicates that the SJE supplies maximum flow rate when the area-average pressure drop across the ejector is zero gauge, and there will be no flow if that pressure drop increases to a certain point.

CHAPTER 4

NUMERICAL EXPERIMENTS TO OPTIMIZE THE SJE

This chapter is devoted to a determination of the optimum geometrical and operating parameters for the SJE configuration being considered. Based on the trends found in the previous chapter, some assumptions will be made. The optimum values of the parameters will then be determined using a univariate search optimization method [22] with initial guesses which, in some cases, are based on the results of the preliminary study conducted in Section 3.6.

4.1 Modified SJE Numerical Model

The following assumptions are made for the new model.

- The orifice diameter (d) is taken to be the same as the SJA diameter (D). This assumption is based on the trends observed in Sections 3.6.1 and 3.6.2 that the dimensionless flow rate has its maximum when d is close to D. Ideally, this means one end of SJA is the vibrating diaphragm and the other end is totally open to the mixing area. Although this geometry cannot be exactly realized in practice, it can be approximated.

- The optimum shroud length (L_e) to shroud diameter (D_e) ratio is found to be approximately 2.7 for the initial configuration shown in Section 3.6.3. The ratio is expected to be different for the final optimum geometry. In order to save computational time, a new L_e value of 16 mm is taken as the starting shroud length for the numerical optimization procedure. The new D_e value is taken to be 3.88 mm, thus the new L_e/D_e value is 4.12.

- The results of section 3.6.5 suggest that the optimum Reynolds number for the peak dimensionless flow rate is approximately 30,000. When the air

density and viscosity are constant, SJE Reynolds number is determined by the shroud diameter (D_e) and primary input velocity amplitude (V_A). Instead of choosing a value of V_A to give a Reynolds number of 30,000, a value of 5 m/s is chosen and used as the initial value for the numerical optimization procedure. This decision was partially due to the desire to make use of previous calculations and hence reduce the computational effort. The new SJE Reynolds number is 1,250 and quite different than the 30,000 from Section 3.6.5. Note, however, that this is just a starting point and, with the iterative univariate search technique, will soon be corrected.

- According to Section 3.6.4, the dimensionless flow rate isn't very sensitive to the input frequency (f). A value of 2,000 Hz is taken as the starting point for the numerical optimization experiment which gives a new Strouhal number of 1.55, which is close to the optimum value of 1.5 found in that section.

- The SJE supplies its maximum flow rate when its area-average pressure drop, Δp, is zero gauge pressure and therefore Δp is assumed to be zero throughout the optimization procedure.

4.2 Optimization Method

The dimensionless flow rate is a function of seven dimensionless groups,

$$\frac{\dot{Q}_s}{D_e^2 V_A} = \phi\left(\frac{d}{D_e}, \frac{D}{D_e}, \frac{L_e}{D_e}, f\frac{D_e}{V_A}, \frac{\rho V_A D_e}{\mu}, \frac{\Delta p}{\rho V_A^2}\right) \tag{A10}$$

It is not the purpose of this study to find the exact expression of this function. The maximum value is going to be estimated numerically. The optimization method used in this chapter is straightforward and similar to the procedure used in the previous chapter. In order to obtain the maximum value of the dependent Pi term, $\frac{\dot{Q}_s}{D_e^2 V_A}$, a particular geometry of the SJE with initial parameters are selected. The local maximum value of the dependent Pi term can be found with respect to the first independent Pi term, $\frac{d}{D_e}$, by changing the value of this Pi term while holding the other independent Pi terms constant. Using the newly found optimum value for the first independent Pi term and the old known values for the other independent Pi terms, the same procedure can be applied to the other independent Pi terms one by one to determine the maximum value of the dependent Pi term in the first iteration. These steps are repeated for the second iteration, and so on. The new maximum of the dependent Pi term is compared with the one from the previous iteration. If the absolute difference is less than 10%, the optimization procedure will end. If not, the iteration continues. This procedure will yield a local maximum. If, however, more than one maximum exists, the second maximum condition will not be obtained. It is assumed that only one maximum occurs.

4.3 Optimum Dimensionless (Pi Term) Values

4.3.1 Iteration I

As mentioned in Section 4.1, the starting values of the parameters for optimization are D_e=3.88 mm, L_e=16 mm, V_A=5 m/s and f=2,000 Hz. The corresponding L_e/D_e, Strouhal number and Reynolds number are 4.12, 1.55 and 1,250, respectively. The optimum values found in this iteration are denoted by "$(\ )_{\Pi}$".

4.3.1.1 Optimum d/D_e

Changing the values of d (or D since $d \approx D$), the results are plotted in dimensionless terms in Figure 4.1.

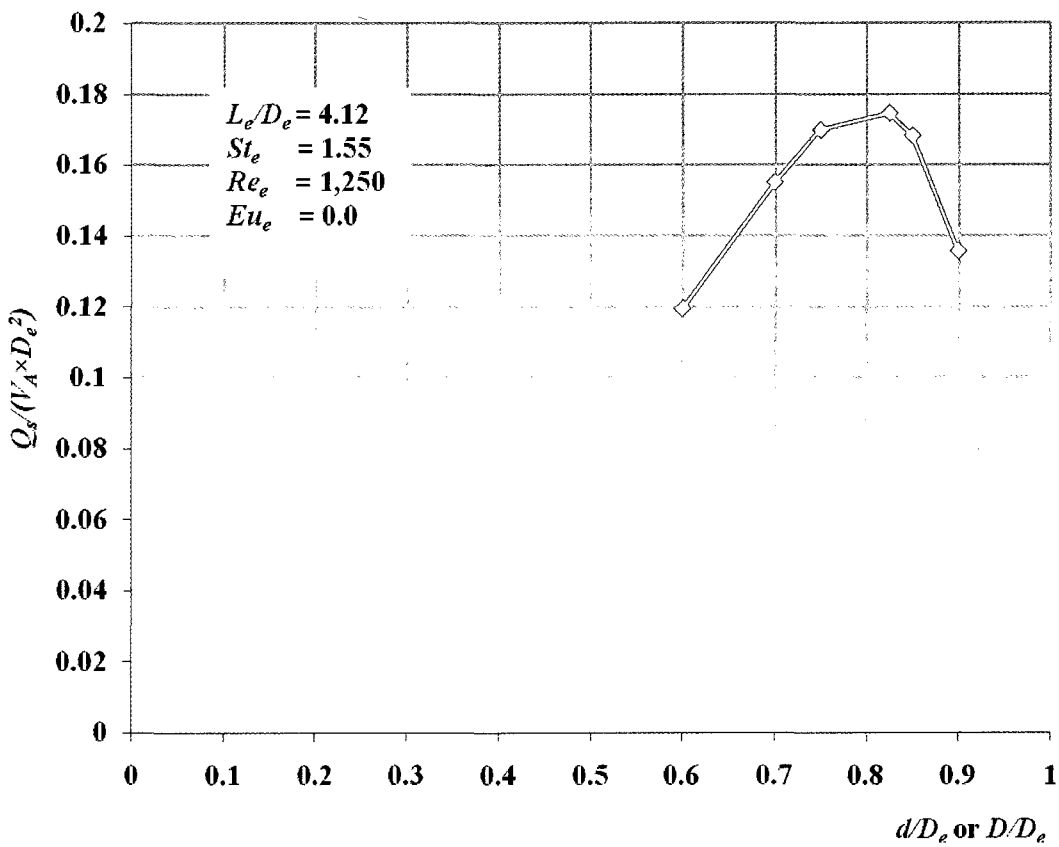

Figure 4.1 Variation of dimensionless flow rate with *d* (or *D*).

The dimensionless flow rate has its maximum value of 0.174 when d/D_e is approximately 0.825. It declines rapidly when d/D_e is either higher or lower than 0.825.

4.3.1.2 Optimum L_e/D_e

The results obtained by keeping d/D_e at its optimum value of 0.825 and changing the shroud length L_e are presented non-dimensionally in Figure 4.2.

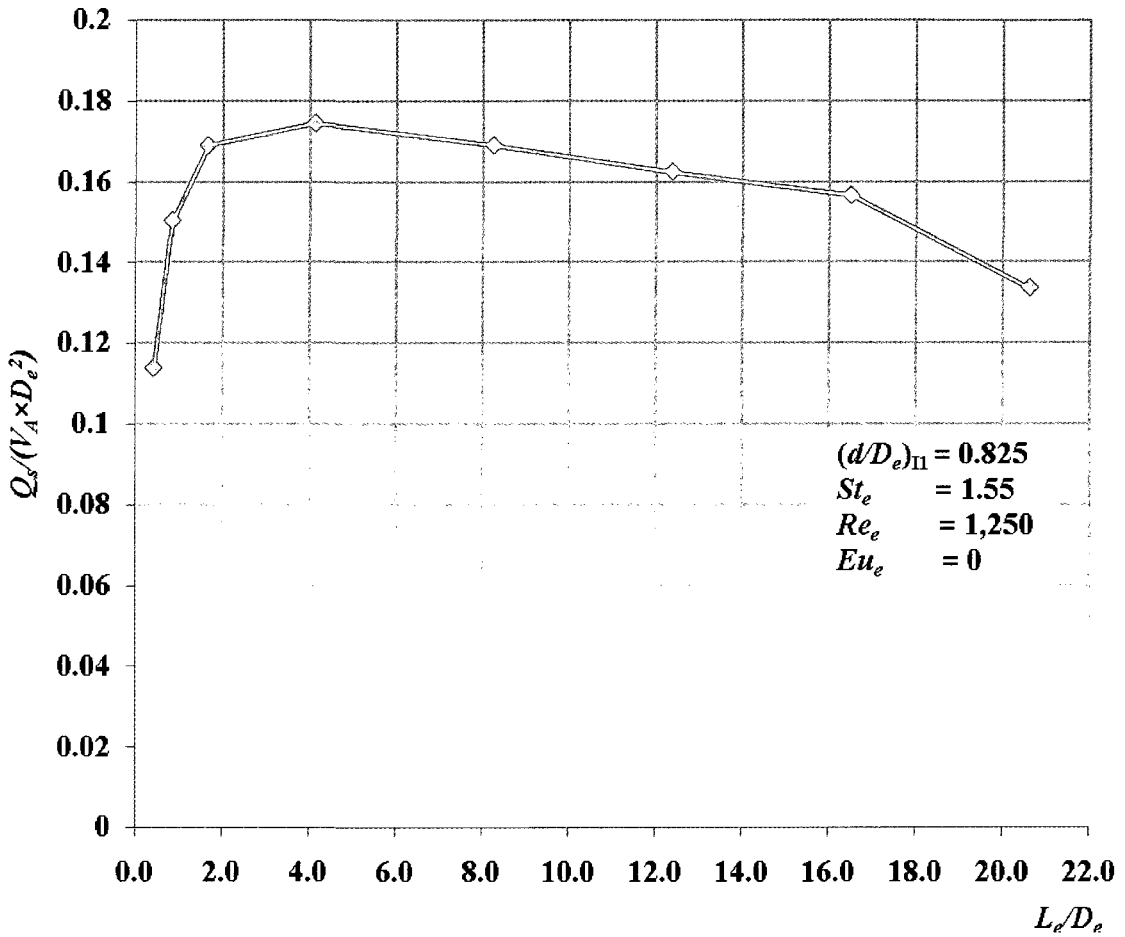

Figure 4.2 Variation of dimensionless flow rate with L_e/D_e.

The dimensionless flow rate increases as L_e/D_e increases. It reaches its maximum then starts declining at a lower rate than that at which it increases. The value of L_e/D_e is 4.12 at the local optimum.

4.3.1.3 Optimum Strouhal Number

The values of d/D_e and L_e/D_e are kept at their optimum values of 0.825 and 4.12, respectively. The Strouhal number is changed by using various frequencies and the dimensionless results plotted in Figure 4.3.

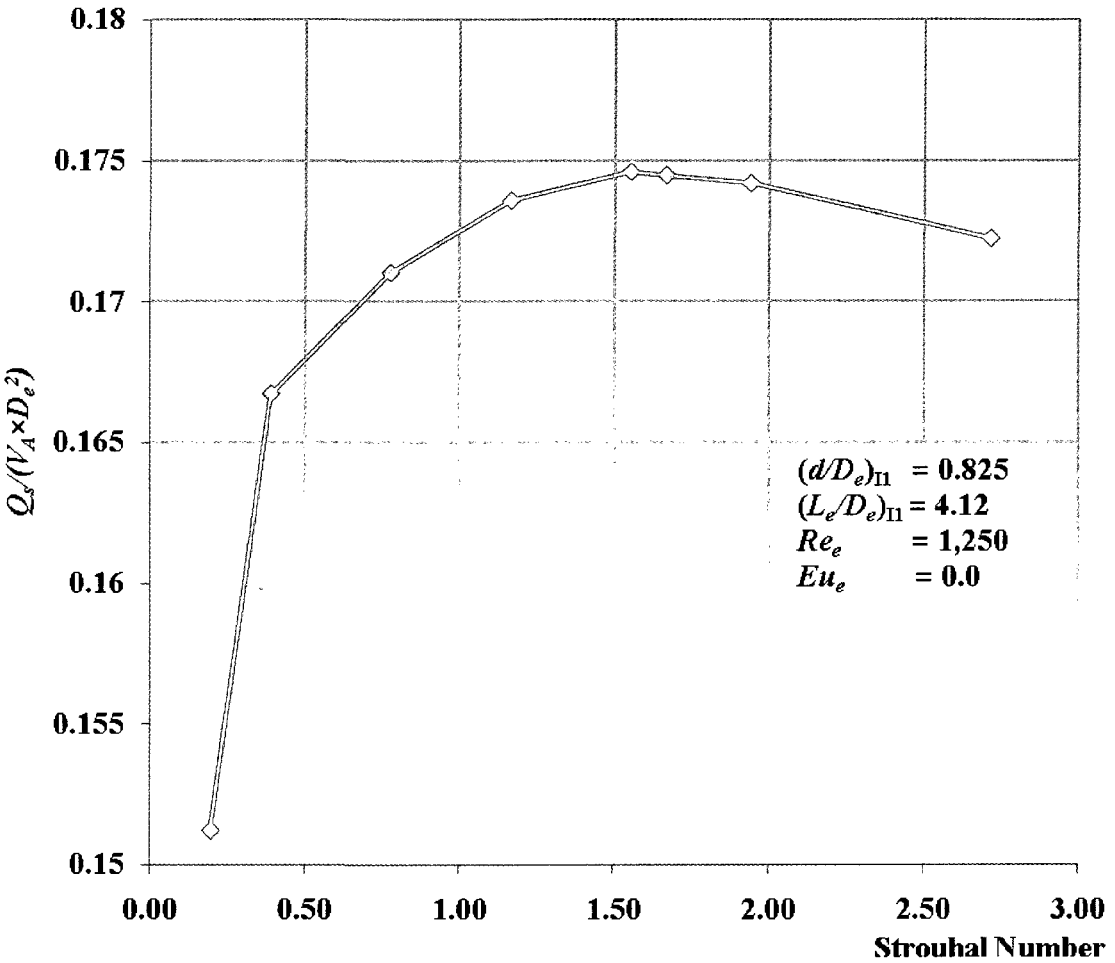

Figure 4.3 Variation of dimensionless flow rate with Strouhal number.

The dimensionless flow rate rises quickly with increasing Strouhal number. It then reaches its peak and decreases with higher Strouhal number. The Strouhal number is approximately 1.55 at the local optimum.

4.3.1.4 Optimum Reynolds Number

The values of d/D_e, L_e/D_e, and St_e are now kept at their optimum values of 0.825, 4.12 and 1.55, respectively. Various Reynolds numbers are selected and the results are plotted in a dimensionless manner in Figure 4.4.

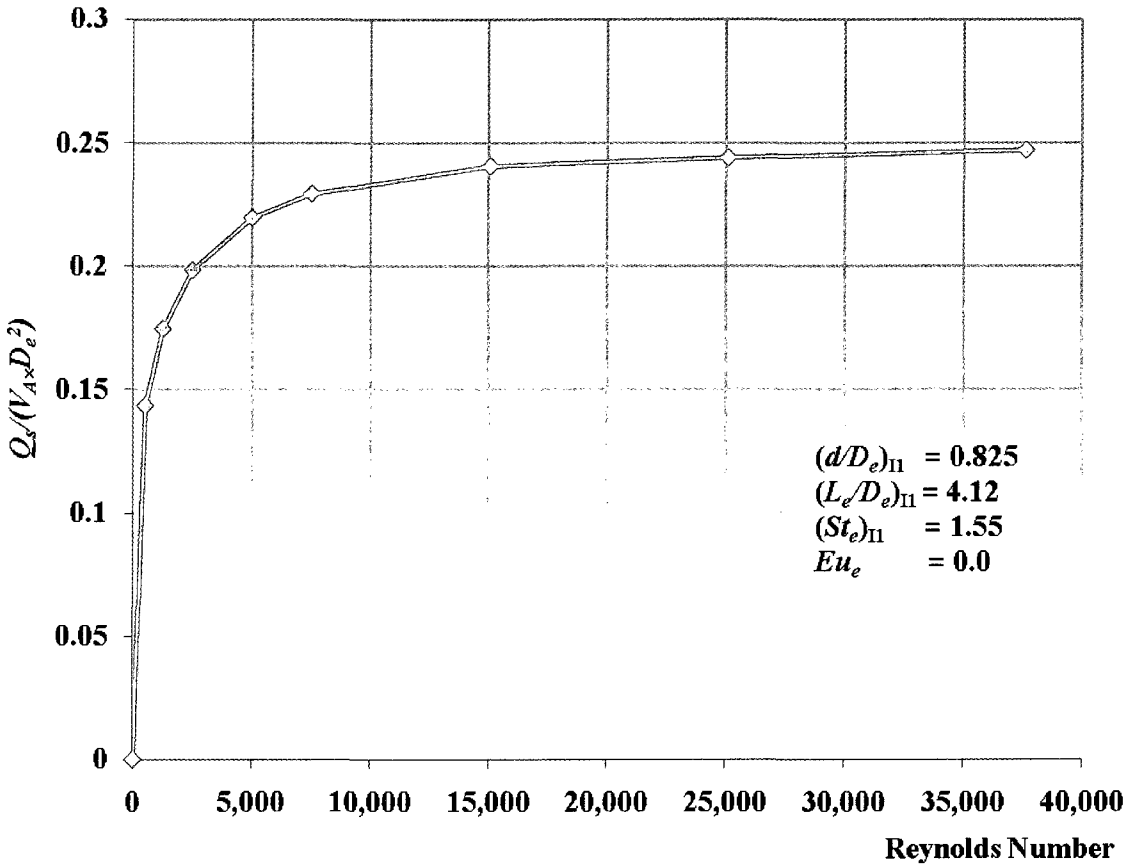

Figure 4.4 Variation of dimensionless flow rate with Reynolds number.

The dimensionless flow rate increases rapidly with increasing Reynolds number and reaches a maximum of 0.25 asymptotically at high Reynolds number. As extremely high Reynolds number values are undesirable from a practical perspective (more energy required), it was decided to arbitrarily choose a value of Reynolds number which give a dimensionless flow rate close to the maximum. This point is taken at a value of 15,060 and the corresponding dimensionless flow rate is 0.241 at the end of this first iteration.

4.3.2 Iteration II

With new local optimum values found from the previous section, the same steps are repeated in this section in order to determine the new optimum values. The optimum values found in this iteration are denoted by "$(\ )_{I2}$". The continuation of the iteration process depends on the difference between the maximum dimensionless flow rate found in this section and the one found in the first iteration.

4.3.2.1 Optimum d/D_e

The values of L_e/D_e, St_e and Re_e are kept at their optimum first iteration values of 4.12, 1.55 and 15,060, respectively. Various d/D_e values are selected for study and the results are presented non-dimensionally in Figure 4.5.

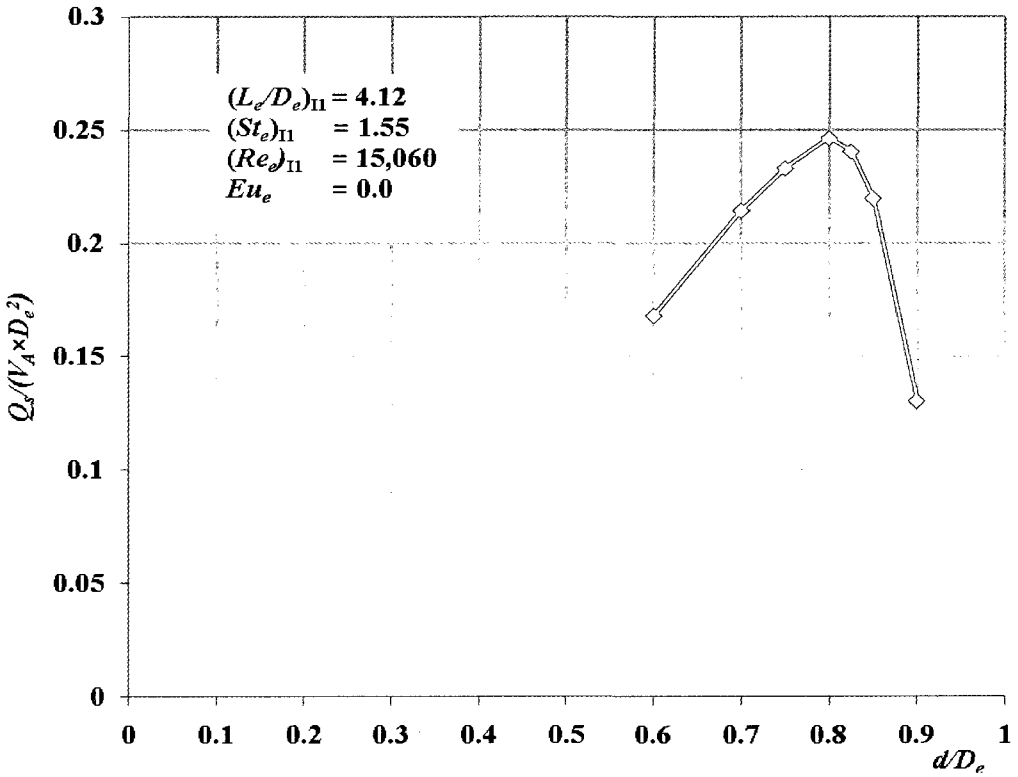

Figure 4.5 Variation of dimensionless flow rate with d/D_e.

Similar to the first iteration, dimensionless flow rate has its local peak of 0.247 with a new optimum value of d/D_e at 0.8. There is only a small change to its old value of 0.825.

4.3.2.2 Optimum L_e/D_e

The values of d/D_e, St_e and Re_e are kept at their current optimum values of 0.8, 1.55 and 15,060, respectively. Various shroud length values are chosen for study and the results are presented in dimensionless terms in Figure 4.6.

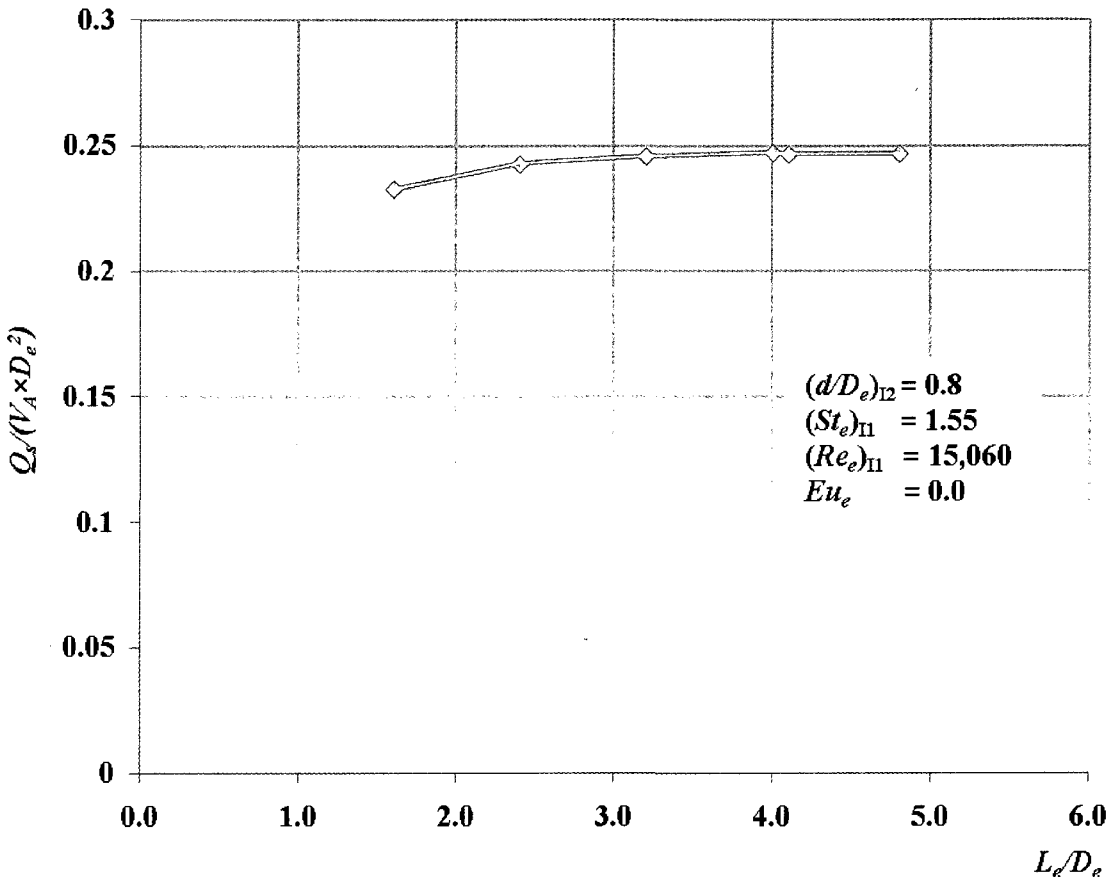

Figure 4.6 Variation of dimensionless flow rate with Le/D_e.

The same trend is found as in the first iteration. A new L_e/D_e optimum is found at 4.0, which is not much different than the old optimum value of 4.1.

4.3.2.3 Optimum Strouhal Number

The values of d/D_e, L_e/D_e, and Re_e are kept at their optimum values of 0.8, 4.0 and 15,060, respectively. Various Strouhal numbers are selected for study and the results are plotted non-dimensionally in Figure 4.7.

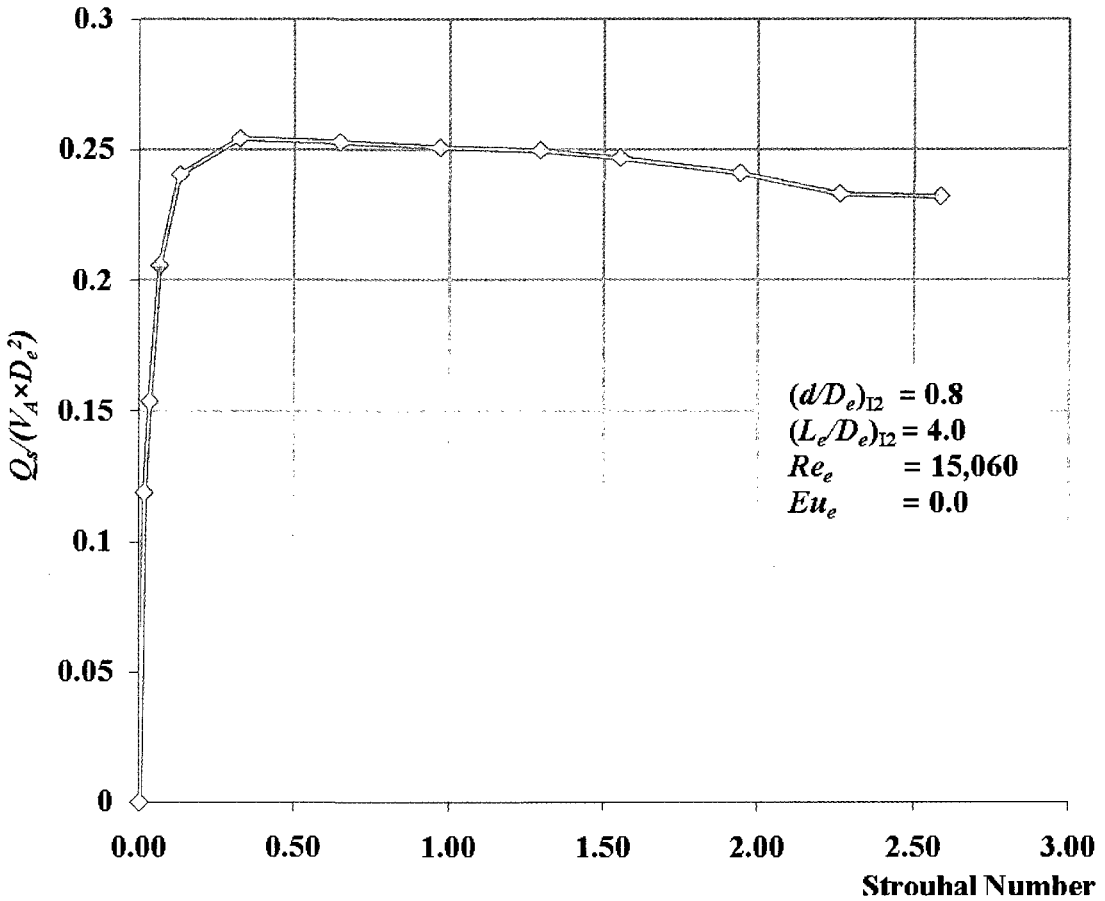

Figure 4.7 Variation of dimensionless flow rate with Strouhal number.

Similar to the trend found in the first iteration, the dimensionless flow rate increases rapidly with increasing Strouhal number. It climbs to its peak value and flattens out with higher Strouhal number. The local optimum value is 0.323, which is considerably lower than 1.55 found in the first iteration. The local dimensionless flow rate increases slightly to 0.255 from 0.241.

4.3.2.4 Optimum Reynolds Number

The values of d/D_e, L_e/D_e, and Strouhal number are kept at their optimum values of 0.8, 4.0 and 0.323, respectively. Various Reynolds numbers are selected for study and the results are presented in dimensionless manner in Figure 4.8.

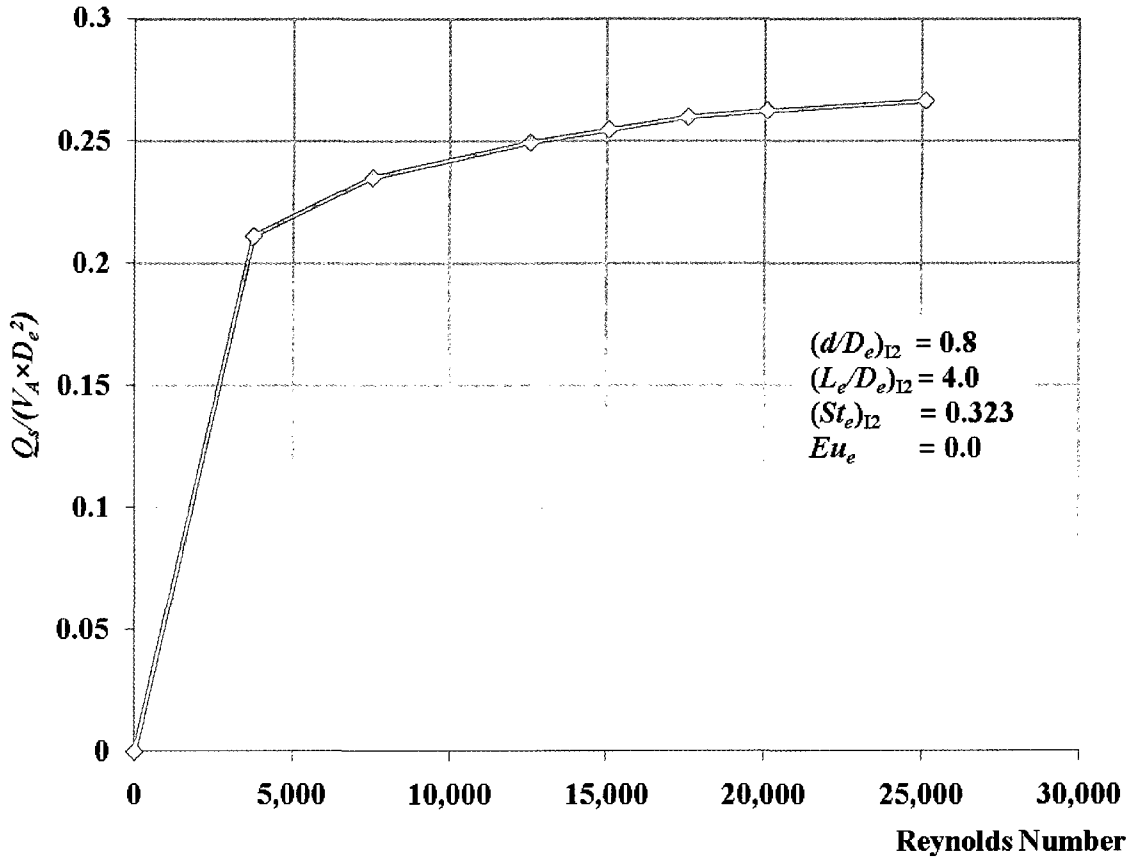

Figure 4.8 Variation of dimensionless flow rate with Reynolds number.

The dimensionless flow rate increases as Reynolds number increases and approaches the maximum asymptotically. Similar to the first iteration, it was decided to take the optimum Reynolds number as 20,000, which gives a dimensionless flow rate value of 0.262 at the end of this second iteration.

4.3.3 Continuation of Iteration

The dimensionless flow rate maximum occurs at 0.241 in the first iteration, while it is 0.262 in the second iteration. The absolute percentage difference between these iterates is 8.7%, which is less than the 10% considered acceptable for practical purposes. The optimization process is concluded at this stage.

4.3.4 Results of Optimization

The numerical approximate optimum operation condition for a general synthetic jet ejector of the geometrical configuration studied here is summarized in Table 4.1.

Table 4.1 General SJE dimensionless groups optimum operating values.

Dimensionless Group (Pi Terms)	Optimum Value
$\frac{\dot{Q}_s}{D_e^2 V_A}$	0.262
d/D_e	0.8
D/D_e	0.8
L_e/D_e	4.0
$f\frac{D_e}{V_A}$	0.323
$\frac{\rho V_A D_e}{\mu}$	20,000
$\frac{\Delta p}{\rho V_A^2}$	0.0

The optimum SJE performance curve is plotted non-dimensionally in Figure 4.9. It can be seen that the dimensionless flow rate is at its maximum with zero gauge pressure difference across the ejector.

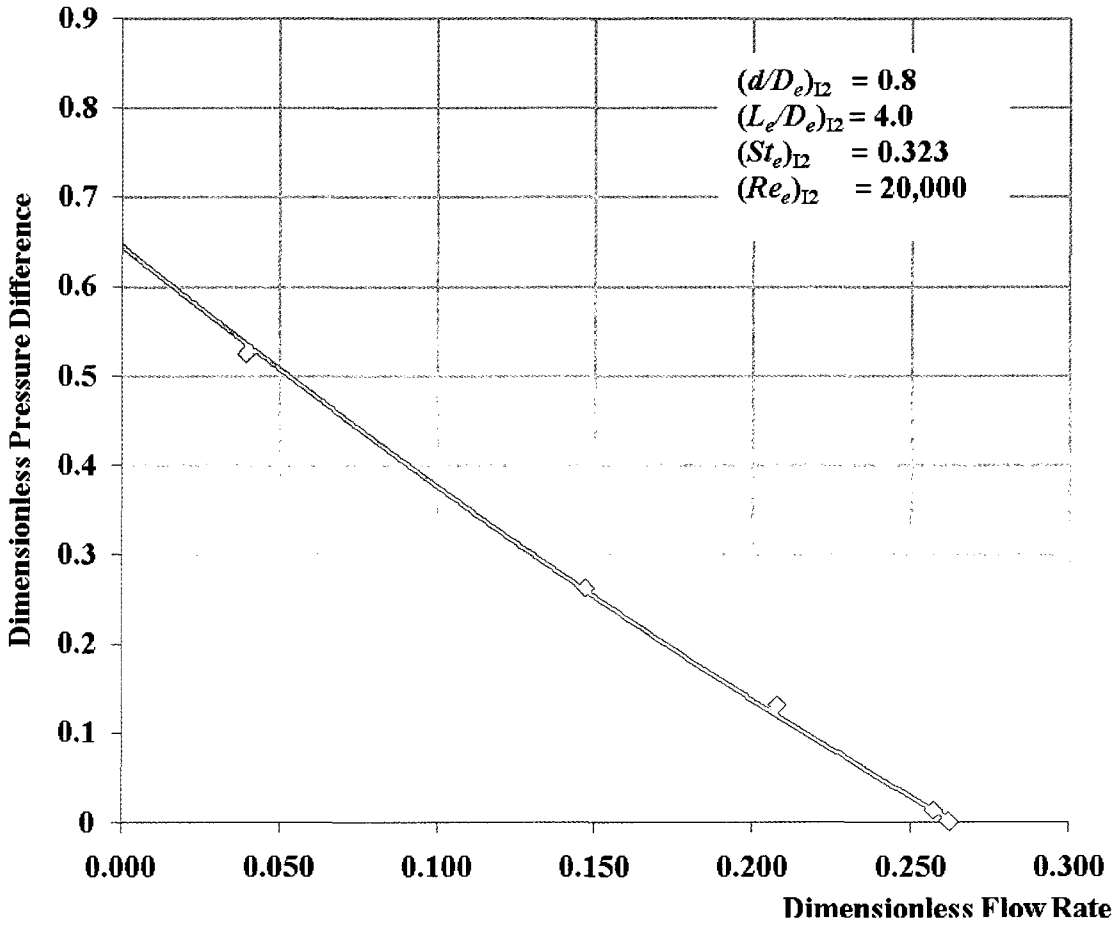

Figure 4.9 Optimum SJE performance curve.

CHAPTER 5

AUTOMOTIVE SEAT VENTILATION FEASIBILITY

In this chapter, the feasibility of the SJE for use in the automotive seat ventilation application will be explored.

5.1 Automotive Seat Ventilation

The automatic seat heating/cooling system has become a desired feature in many automobile models. Traditionally, one or two blowers are installed under the seat to either push or pull air through the seat layers for ventilation. The benefit is countered by the vibration and noise from the blower, not to mention the cost and durability of the blower. Researchers have been searching for more efficient and reliable mechanical systems to replace the blowers. The SJE studied in this project is a possible replacement for the blower. In order to replace the blower, the SJEs must have similar capability to that of the blower. The blower generates a flow of air by creating a pressure difference. In the next section, air flow rate/pressure requirement for a typical automotive seat ventilation system is presented and compared with the SJEs performance.

5.2 Proposed SJE for Automotive Seat Ventilation

Test results for a typical car seat air flow are presented in Figure 5.1. As the air flow rate increases, additional pressure is required. This is referred to as the system curve in pump selection.

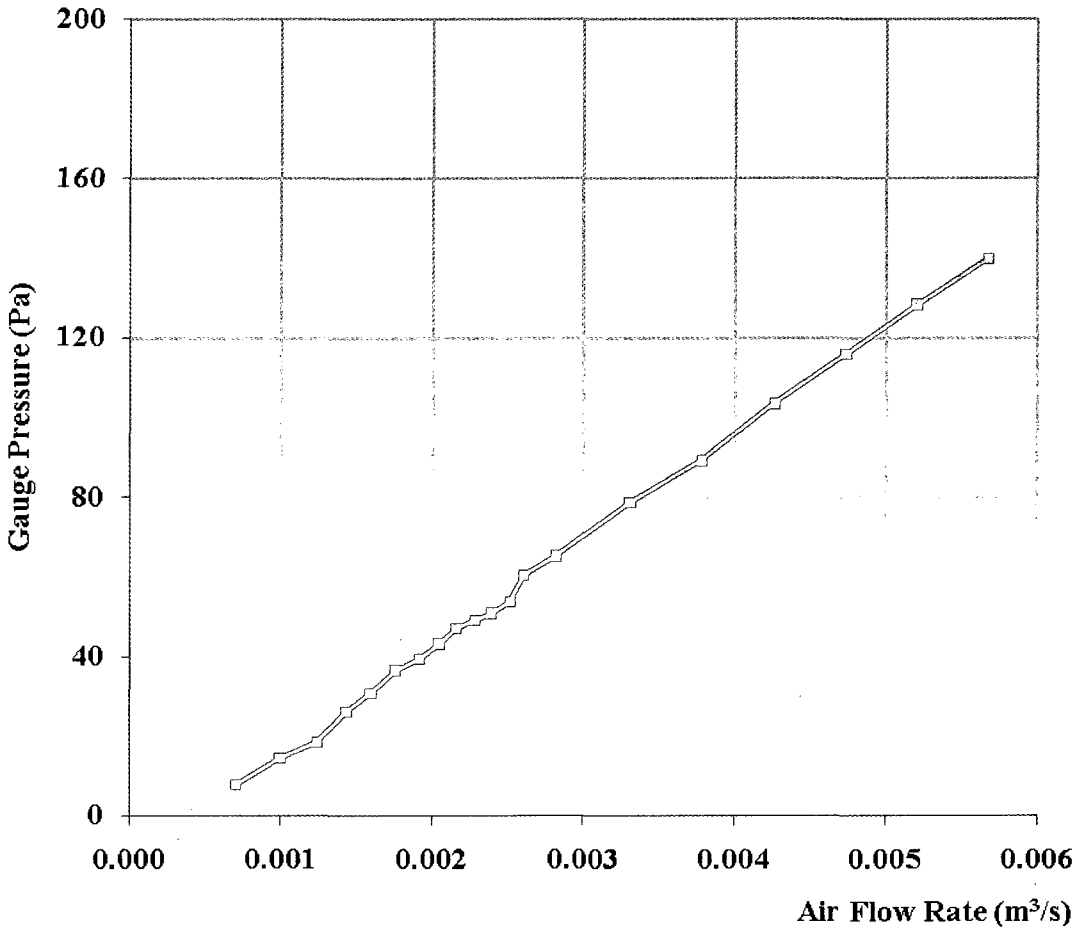

Figure 5.1 Typical automotive seat air flow system curve.

The performance curve for the optimum SJE is plotted in dimensionless terms in Figure 4.9. In order to compare the SJE to the above system curve, it is necessary to use dimensional quantities which are governed by the physical constraints of the application. The dimensionless flow rate is $\frac{\dot{Q}_s}{D_e^2 V_A}$, which implies, under optimum conditions, that the larger the shroud diameter, D_e, the higher the flow rate, $\dot{Q}_s$. Due to space limitations

around the seat, the maximum length for the SJE shroud is 80 mm, which gives the maximum shroud diameter of 20 mm. From the values of optimum Reynolds number and Strouhal number, the optimum primary velocity amplitude, V_A, and driving frequency, f, are 15.5 m/s and 250 Hz, respectively. The resulting performance curve is plotted in Figure 5.2.

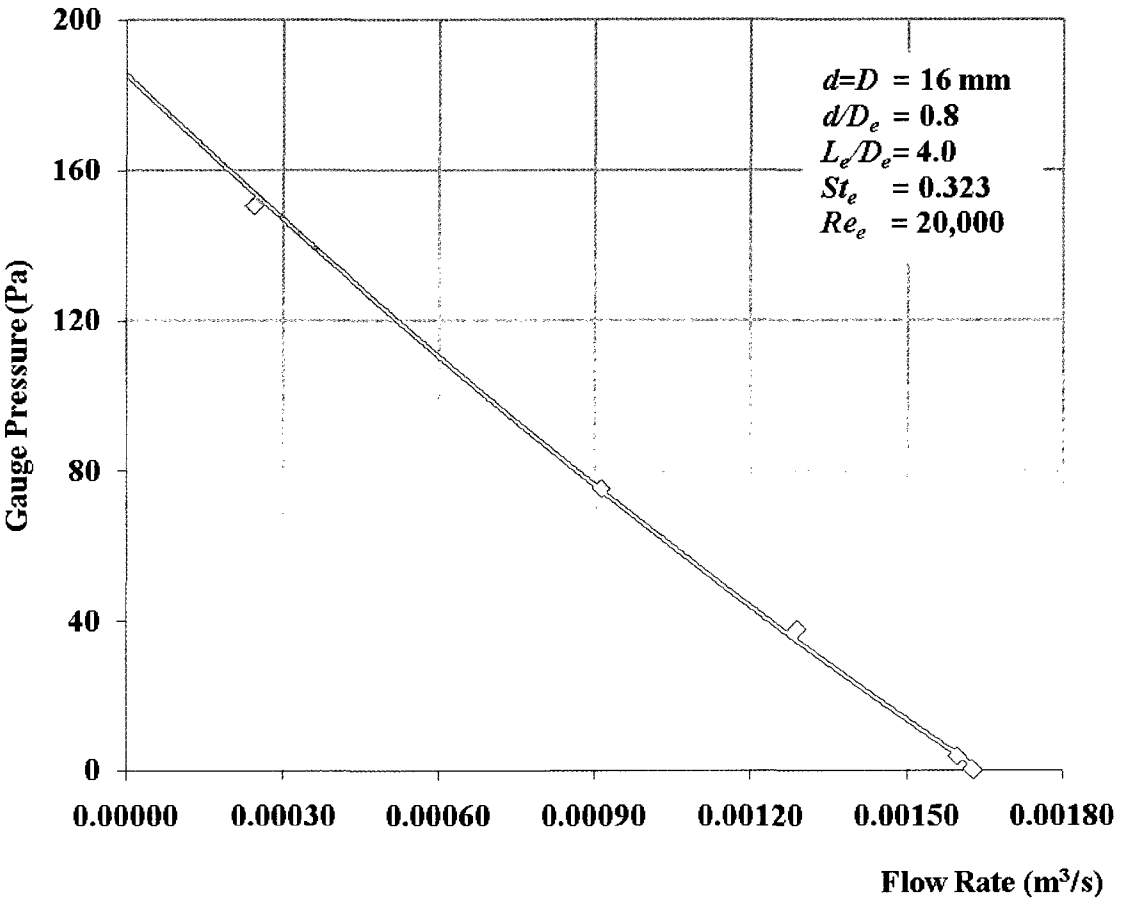

Figure 5.2 Single optimum SJE performance curve for automotive application.

The maximum gauge pressure that can be delivered is close to 180 Pa, above the 140 Pa gauge pressure that the system needs. The maximum flow rate that the SJE can create however is only 0.00163 m^3/s, which indicates there will be more than one SJE needed for this application. When a number of SJEs are installed in parallel, the flow rate will be multiplied by the number of SJEs while the pressure delivered will be the same.

The results with 3, 5 and 10 SJEs installed in the system are plotted in Figure 5.3 with the system curve requirement.

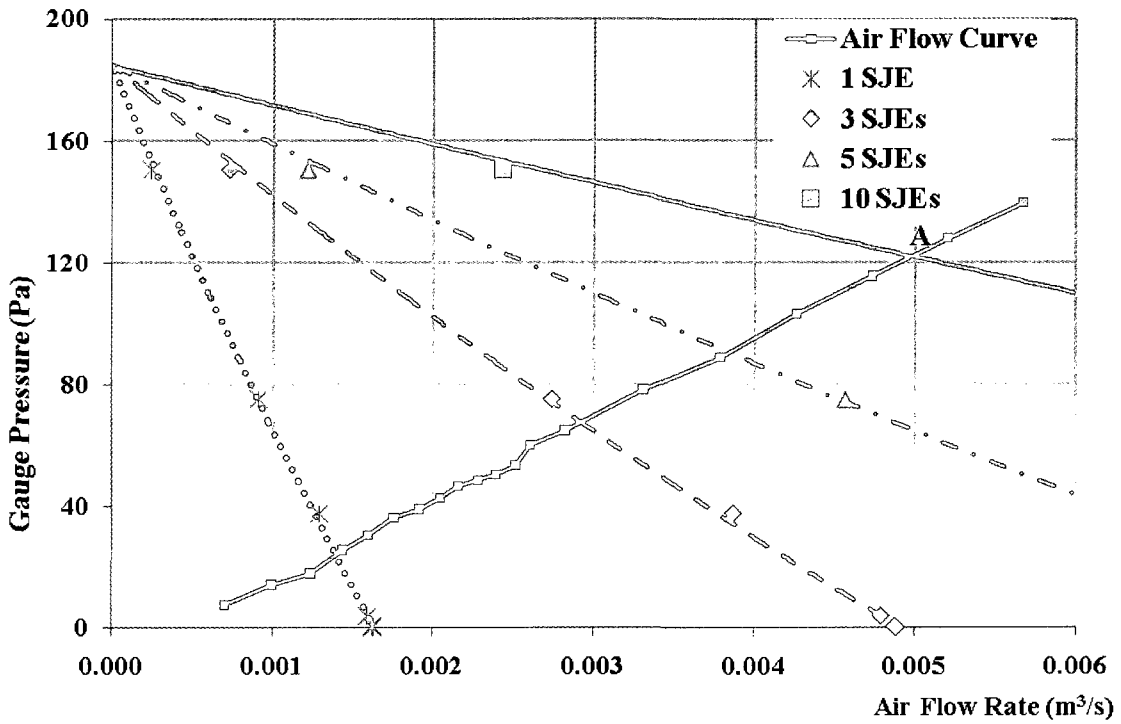

Figure 5.3 Automotive air ventilation system curve.

In the case of 10 SJEs, each one is required to deliver a gauge pressure of 120 Pa, which is about 66.7% of the maximum of 180 Pa. At the system operating point, A, the highest flow rate of all three cases is delivered.

Based on the pressure that the SJE delivers and the flow rate it provides, it is possible to use this technology in the automotive ventilation application. A total number of 10 SJEs are needed for this application. The optimum geometric dimensions and operating parameter values for the SJE are summarized in Table 5.1.

Table 5.1 Optimum SJE for automotive air (at STP) ventilation application.

Synthetic Jet Ejector Parameters	Optimum Values
SJA orifice diameter, d (m)	0.016
SJA diameter, D (m)	0.016
SJE shroud diameter, D_e (m)	0.02
SJE shroud length, L_e (m)	0.08
Input frequency, f (Hz)	250
Primary inlet velocity amplitude, V_A (m/s)	15.5

CHAPTER 6

CONCLUSIONS AND RECOMMENDATIONS

6.1 Conclusions

The performance of an axisymmetric synthetic jet ejector configuration, excluding the actuator, is investigated numerically using a 2-D approximation. An efficient numerical model is developed based on grid size, grid structure, and time step size. All simulations use the $k-\varepsilon$ turbulence model along with the second-order upwind scheme for spatial discretization and second-order implicit scheme for time advancement. A 0.1% difference criterion is used to determine the existence of a time periodic state of the outlet flow rate and a tolerance of 10% in the flow rate is used in determining the optimal SJE parameters.

With dimensional analysis, the SJE is found to have an optimum operating condition with the orifice diameter the same size as the actuator diameter. The ratio between the orifice diameter and the shroud diameter is 0.8, while that between the shroud length and shroud diameter is 4. The optimum Strouhal number and Reynolds number are 0.323 and 20,000, respectively. The SJE provides its maximum flow rate with zero gauge pressure across the ejector.

The optimum SJE with dimensions consistent with the automotive seat application has an orifice diameter and actuator diameter of 16 mm, shroud diameter of 20 mm, shroud length of 80 mm, a driving frequency of 250 Hz, and primary input velocity amplitude of 15.5 m/s. It was found that 10 of these optimum SJEs in parallel is a possible alternative for the blower for automotive seat ventilation application.

6.2 Recommendations

The following recommendation for future works are made.

- Conduct experiments to provide data for comparison with the numerical results.
- Consider what SJ actuator is required to achieve the optimum velocity amplitude with optimum frequency and diameter.
- Investigate the improvement of SJE performance using various shroud shapes [12], novel actuators [9], and non-sinusoidal primary inlet velocity profile [6].
- The formation criterion for a free synthetic jet is that its Strouhal number, $f\frac{\pi d}{V_A}$, defined by Equation (2.7), must be less than 0.16 for a round orifice. It is expected that the formation criterion for the synthetic jet ejector will be different from the free synthetic jet. Future work should focus on determining this criterion and its relationship with the optimum Strouhal number.
- The SJE with optimum parameters found in this study does not deliver the maximum suction pressure at the secondary inlet. Future research should focus on finding the optimum parameters for maximum suction pressure.

Appendix A

Dimensional Analysis

The main focus of this study is to determine the performance curves for the SJE. This involves a determination of the secondary inlet flow rate, $\dot{Q}_s$, which is a function of the following variables,

$$\dot{Q}_s = \varphi(d, D, D_e, L_e, V_A, f, \rho, \mu, \Delta p) \tag{A1}$$

where d= synthetic jet ejector orifice diameter

D=synthetic jet actuator diameter

D_e=SJE shroud diameter

L_e=SJE shroud length

V_A=SJE primary inlet velocity amplitude

f=SJ diaphragm driving frequency

ρ =air density

μ =air dynamic viscosity

Δp =area-average pressure drop across the SJE

Using mass M, length L and time T as basic dimensions, all variables can be expressed in terms of the basic dimensions as follows.

$$\dot{Q}_s \equiv m^3/s \equiv m^3 s^{-1} \equiv L^3 T^{-1}$$

$$d \equiv m \equiv L$$

$$D \equiv m \equiv L$$

$$D_e \equiv m \equiv L$$

$$L_e \equiv m \equiv L$$

$$V_A \equiv m/s \equiv ms^{-1} = LT^{-1}$$

$$f \equiv 1/T \equiv T^{-1}$$

$$\rho \equiv kg/m^3 \equiv kg\ m^{-3} \equiv ML^{-3}$$

$$\mu \equiv N\,s/m^2 \equiv \left(kg\ \ m/s^2\right)\ sm^{-2} = kg\ s^{-1}m^{-1} \equiv MT^{-1}L^{-1}$$

$$\Delta p \equiv N/m^2 \equiv \left(kg\ \ m/s^2\right)\ m^{-2} \equiv ML^{-1}T^{-2}$$

According to the Buckingham Pi theorem, if an equation involving k variables is dimensionally homogeneous, it can be reduced to a relationship among k-r independent dimensionless products, known as "Pi terms", where r is the minimum number of basic dimensions required to describe the variables [13]. Based on the theorem, there will be seven (10-3) Pi terms. Starting with the dependent variable and combining it with repeating variables ρ, D_e and V_A to form the first Pi term,

$$\prod_1 = \dot{Q}_s \rho^{c1} D_e^{c2} V_A^{c3} \tag{A2}$$

Because it is dimensionless, this implies that,

$$\left(L^3T^{-1}\right)\left(ML^{-3}\right)^{c1}\left(L\right)^{c2}\left(LT^{-1}\right)^{c3} = M^0L^0T^0$$

The exponents c1, c2 and c3 can be determined by solving the following set of equations

$$\begin{cases} c1 = 0 \\ 3 - 3c1 + c2 + c3 = 0 \\ -1 - c3 = 0 \end{cases}$$

It follows that c1=0, c2=-2, c3=-1, therefore,

$$\prod_1 = \frac{\dot{Q}_s}{D_e^2 V_A} \tag{A3}$$

If the same procedure is repeated for the remaining non-repeating variables, the Pi terms are

$$\prod_2 = \frac{d}{D_e} \tag{A4}$$

$$\prod_3 = \frac{D}{D_e} \tag{A5}$$

$$\prod_4 = \frac{L_e}{D_e} \tag{A6}$$

$$\prod_5 = f\frac{D_e}{V_A} \tag{A7}$$

$$\prod_6 = \frac{\rho V_A D_e}{\mu} \tag{A8}$$

$$\prod_7 = \frac{\Delta p}{\rho V_A^2} \tag{A9}$$

Thus, the required secondary inlet flow rate can be studied by using the relationship

$$\frac{\dot{Q}_s}{D_e^2 V_A} = \phi\left(\frac{d}{D_e}, \frac{D}{D_e}, \frac{L_e}{D_e}, f\frac{D_e}{V_A}, \frac{\rho V_A D_e}{\mu}, \frac{\Delta p}{\rho V_A^2}\right) \tag{A10}$$

The results will be valid for any SJEs that are geometrically similar. In fluid mechanics, the dimensionless group $f\frac{d}{V}$ is referred as Strouhal number, *St*, while $\frac{\rho V d}{\mu}$ is called Reynolds number, *Re*, and $\frac{\Delta p}{\rho V^2}$ is Euler number, *Eu*. Hence, for the

synthetic jet ejector, its Strouhal number, St_e, is defined as $f\frac{D_e}{V_A}$, its Reynolds number, Re_e, is given by $\frac{\rho V_A D_e}{\mu}$, and the its Euler number, Eu_e, is calculated as $\frac{\Delta p}{\rho V_A^2}$.

In order to validate the dimensional analysis results, two SJEs with different geometric dimensions were selected and their dimensionless flow rates compared. More details and the results are shown in Table A.1.

Table A.1 Comparison of SJEs with various geometric dimensions.

	#1 Synthetic jet ejector	**#2 Synthetic jet ejector**
Orifice diameter, d (mm)	3.104	15.52
SJ actuator diameter, D (mm)	3.104	15.52
Shroud diameter, D_e (mm)	3.88	19.4
Shroud length, L_e (mm)	15.52	77.6
V_A (m/s)	50	10
f (Hz)	2,000	80

These dimensional values give independent dimensionless values d/D_e=0.8, D/D_e=0.8, L_e/D_e=4.0, St_e=0.155, Re_e=12,500 and Eu_e=0.0 for both synthetic jet ejectors #1 and #2. The dependent dimensionless quantity $\frac{\dot{Q}_s}{D_e^2 V_A}$ is found to be 0.236 for ejector #1 and 0.228 for ejector #2. The absolute percentage difference between the dependent dimensionless flow rates is less than 3.4%. The same dimensional analysis procedure was applied to the synthetic jet flow field in Appendix B for turbulence model validation, and the results agree well with the experimental data. Therefore, it is believed that all variables have been considered and the dimensional analysis is considered to be valid.

Appendix B

$k-\varepsilon$ Turbulence Model Validation

Over the years, a number of researchers [3,9,11] have used the $k-\varepsilon$ turbulence model in the CFD analysis of the synthetic jet flow field. It is reasonable to expect that this model would also be valid for the synthetic jet ejector flow field investigation. It is the turbulence model used to obtain the results included in this study. However, for steady jets the $k-\Omega$ turbulence model has been found to give better agreement with experimental results than the $k-\varepsilon$ model [25]. In order to evaluate the $k-\Omega$ model and compare with the $k-\varepsilon$ model, the results of numerical solutions of a synthetic jet flow field with both turbulence models will be compared with the most recent experimental results obtained by Eiliat [1].

Eiliat [1] studied the synthetic jet flow field with orifice diameters of 10 mm and 15 mm at frequencies of 10 Hz and 20 Hz. The case of a 15 mm orifice diameter and 20 Hz input frequency is simulated. The flow field area investigated was about 100 mm X 300 mm. A real size simulation would take weeks of computational time to complete. In order to save computational time and still have the same results, dimensional analysis similar to the SJE in Appendix A is performed here, and the simulation model has been scaled down to one fifth $\left(1/5^{th}\right)$ of the original size, based on the same Reynolds number and Strouhal number for the synthetic jet. Therefore, the calculation domain is 21 mm X 25 mm with orifice diameter of 3 mm. A value of 13.2 m/s is taken as the primary inlet velocity amplitude, and the driving frequency is 500 Hz. As shown in Figure B.1, a mesh is created with the grid lines clustered near the inlet. More details for grid structure can be found in Chapter 3. Suitable boundary conditions are prescribed as in Figure B.2.

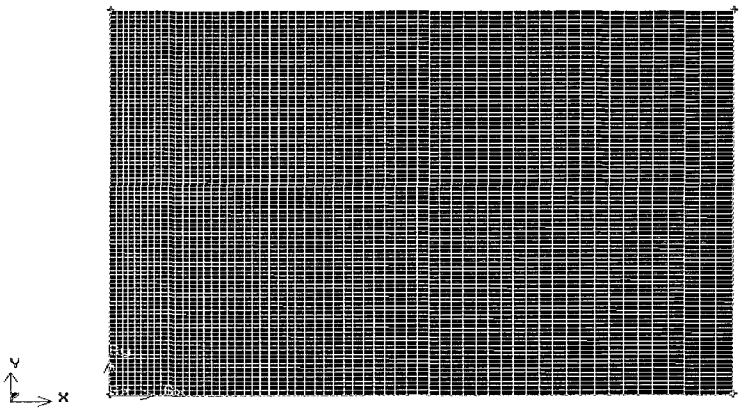

Figure B.1 Synthetic jet flow field computational mesh.

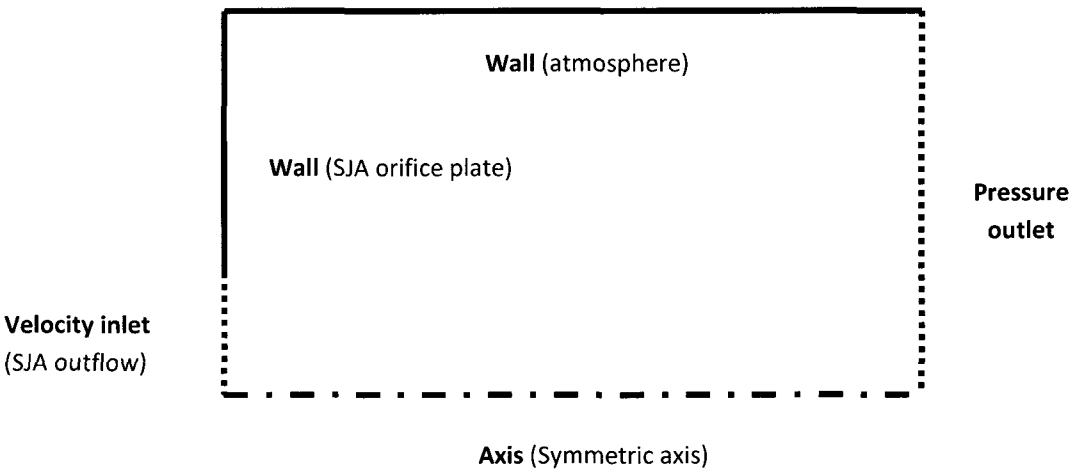

Figure B.2 Boundary conditions for computational domain.

Both the $k-\varepsilon$ and $k-\Omega$ models are used to simulate the flow field. A second-order upwind scheme is used for the spatial discretization and an implicit method is used for time advancement..

The numerical results are compared with experimental results for time-averaged centreline velocity and mean velocity profiles taken at $d/2$ and $11d/4$ downstream from the orifice. As shown in Figure B.3, both models agree with the experiment in the region very close to the synthetic jet actuator exit, about one orifice diameter away. Further downstream, the discrepancy between these two turbulent models is greater. When a

finer mesh (4 times the original grid points) is applied for the same calculation domain, the results for the $k-\varepsilon$ model do not change very much, which means its solution is mesh independent. For the $k-\Omega$ model, the results for the same two grids that are used in the $k-\varepsilon$ study do not lie on top of each other. As an even finer (16x or 32x) mesh is used for the $k-\Omega$ model, the solution keeps changing, which means it is mesh dependent. This indicates that either more grid points are needed or a more complex grid structure is needed. In any case, the finest $k-\Omega$ results are no better than the $k-\varepsilon$ results when compared with the experimental data. Also the $k-\varepsilon$ results are achieved with considerably less computational effort.

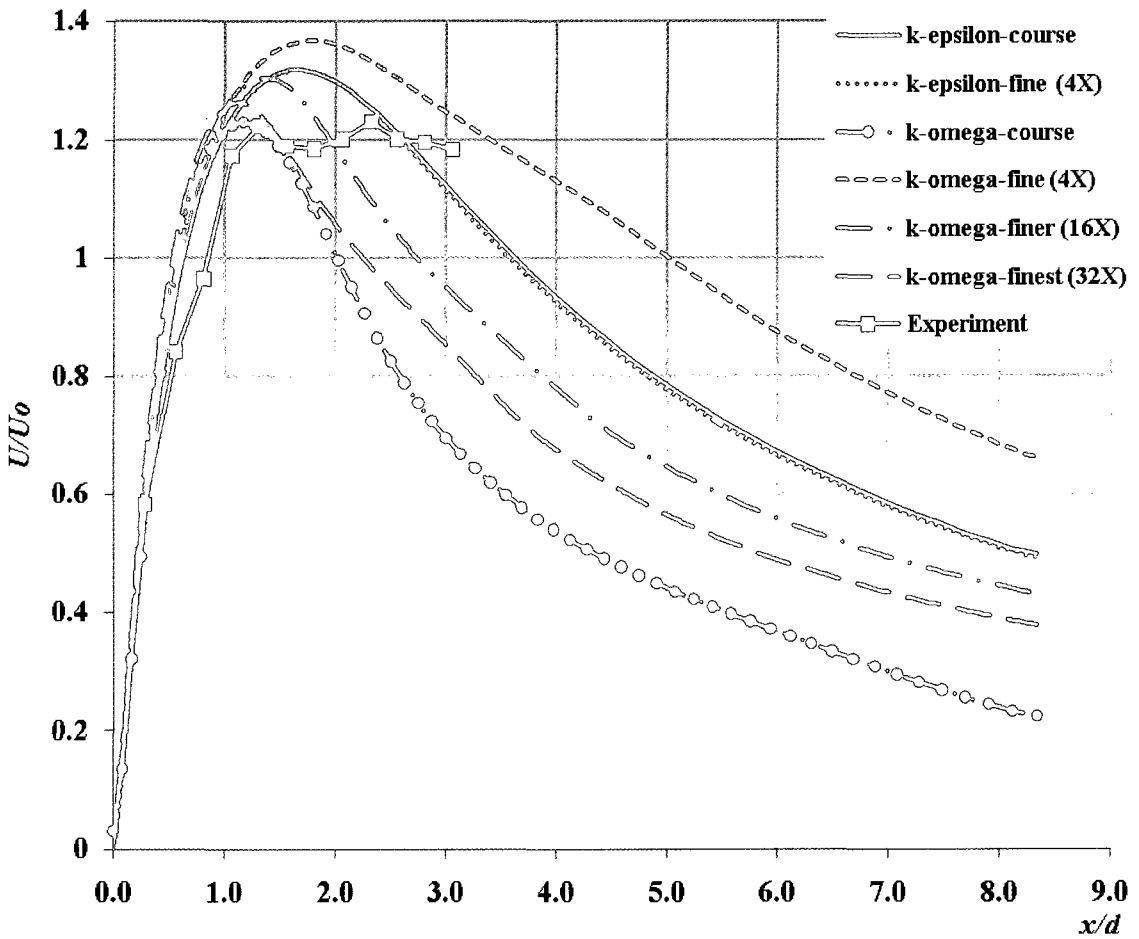

Figure B.3 Comparison of time-averaged centreline velocity versus downstream distance from the exit.

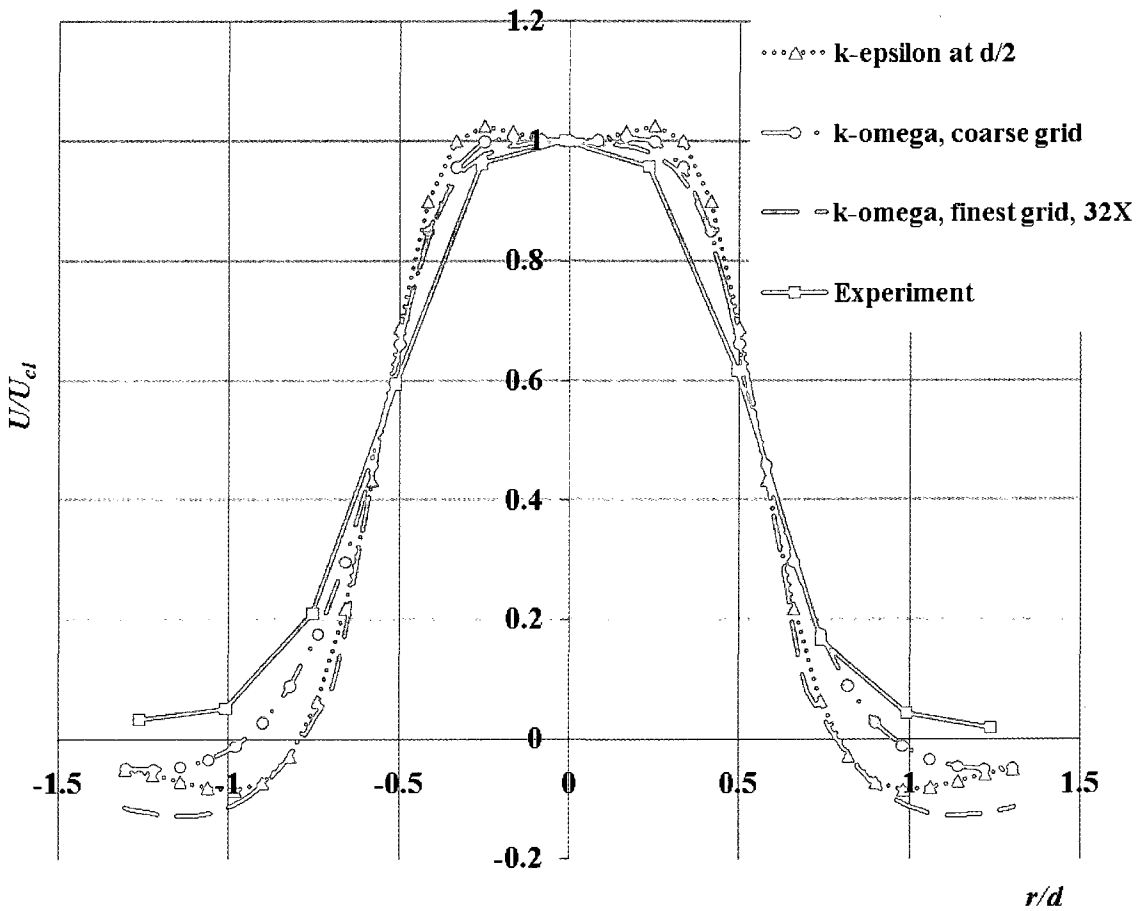

Figure B.4 Comparison of mean velocity profile in the radial direction taken at d/2 downstream from orifice.

Figure B.4 shows the mean velocity profiles taken at d/2 distance downstream from the orifice. In this near orifice region, both models agree well with the experiment. There is a peak of the mean velocity near the centreline. Away from it, the mean velocity goes to negative because of the entrainment. Both models can capture those characteristics as reported in other studies [8, 19].

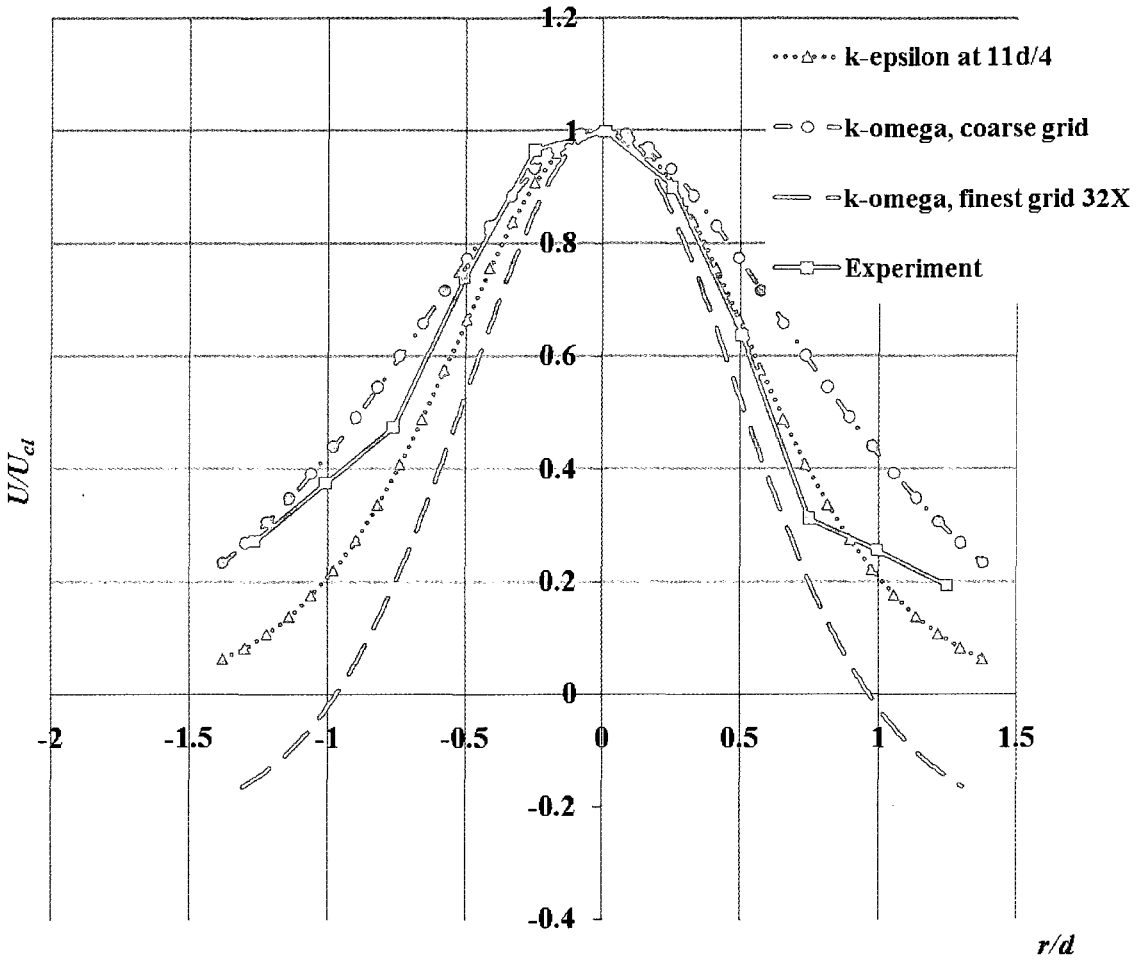

Figure B.5 Comparison of mean velocity profile in the radial direction taken at 11d/4 downstream from orifice.

When the same characteristic is compared further away from the orifice as depicted on Figure B.5, it is clear to see the difference between these models, and the variations between coarse grid and fine grid of the $k-\Omega$ model. It shows that the $k-\Omega$ model results are grid size dependent. Furthermore, the $k-\varepsilon$ model is more accurate than the $k-\Omega$ model prediction at this location.

Based on the above findings, the $k-\varepsilon$ model is justified for use in this project.

Appendix C

Numerical Solution - Fluent Setup

This appendix shows the Fluent setup for all the simulations performed in this study. It has been divided into steps, which are in the order in which Fluent [2] was setup and run.

1. Read in mesh file from Gambit and examine its quality.

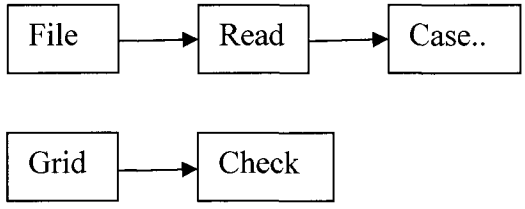

2. Scale the grid size and change the length unit if necessary.

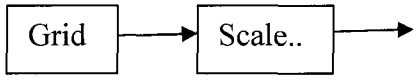

3. Load the User Defined Function (UDF).

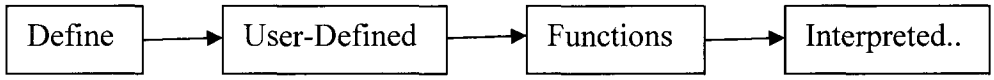

The source file containing the UDF can then be read in. The purpose of the code is to specify the primary inlet velocity function, $V_p(t) = V_A \sin(2\pi f t)$, and is written in C Language but saved as a text file to be read in. The following is an example of the code with 5 m/s velocity amplitude and 2,000 Hz frequency. It is also included on the Data CD.

==========beginning of the code==========

```
#include "udf.h"
DEFINE_PROFILE(unsteady_velocity, thread, position)
{
        face_t f;
```

```
    real t = CURRENT_TIME;

    begin_f_loop(f, thread)
    {
    F_PROFILE(f, thread, position) = 5*sin(2*3.141592*2000*t);
    }
    end_f_loop(f, thread)
}
```

==========end of code==========

4. Select solver.

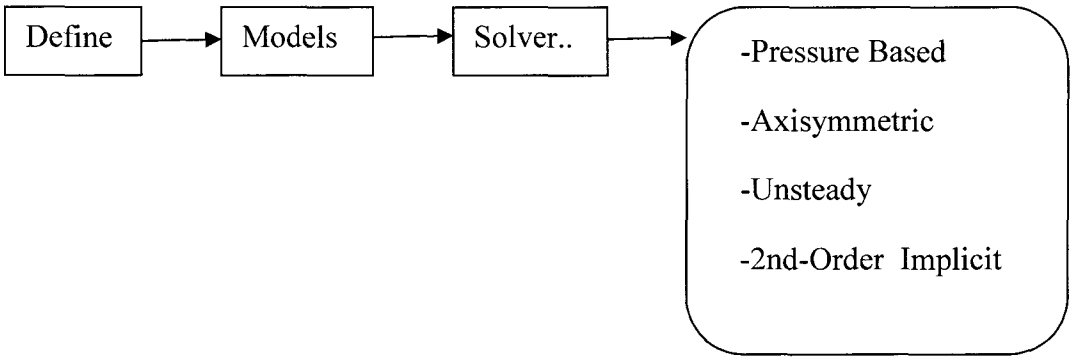

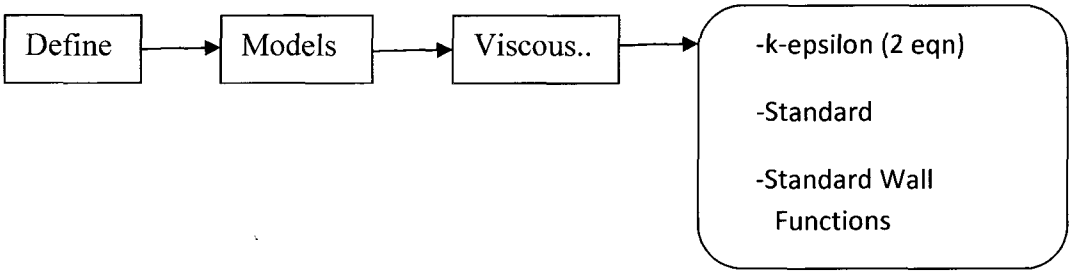

5. Change material properties.

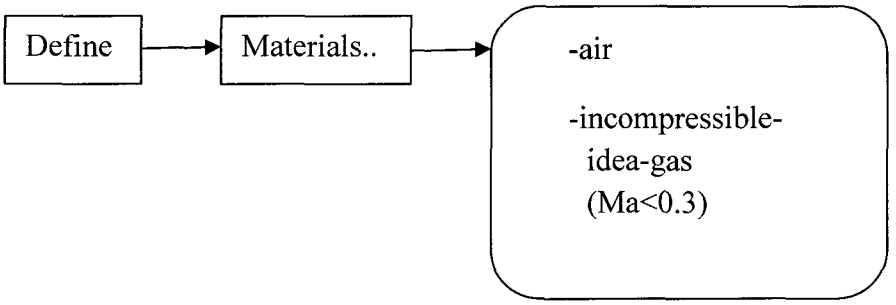

6. Define boundary conditions.

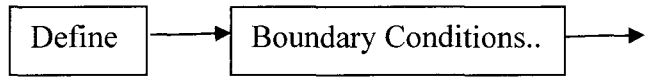

Make sure the boundary conditions have been defined correctly in Gambit.

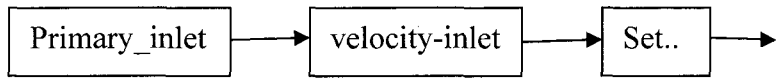

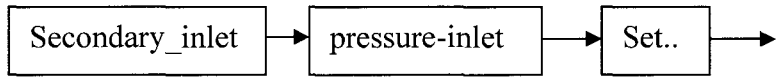

Change gauge pressure if necessary.

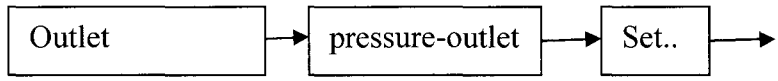

The turbulence intensity and length scale are used for specifying the turbulence characteristics for all inlets and the outlet. The turbulent intensity is assumed to be 1%, while the turbulent length scale is calculated as $0.07L$. The characteristic length L for the primary inlet is the orifice diameter d, for the outlet is shroud diameter D_e, and is the hydraulic diameter (D_e-D) for the secondary inlet.

The gauge pressure of the secondary inlet is altered from a zero value, which corresponds to maximum flow, in order to determine the effect of Euler number on the dimensionless flow rate. It was changed to a negative value to simulate the result of resistance for determining the SJE performance curve.

7. Run the CFD simulation using second-order discretization.

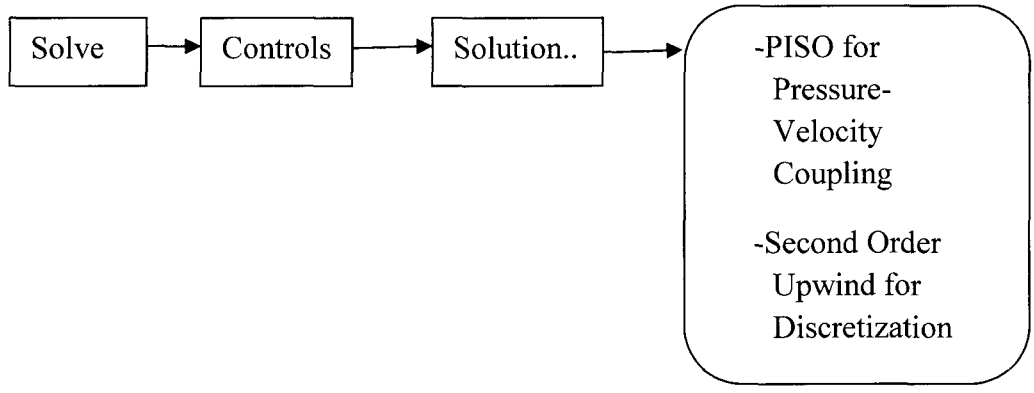

8. Initialize the simulation.

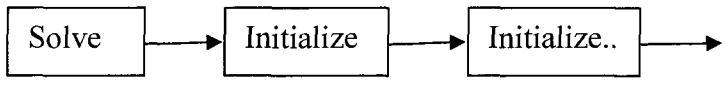

9. Monitor convergence with residuals history.

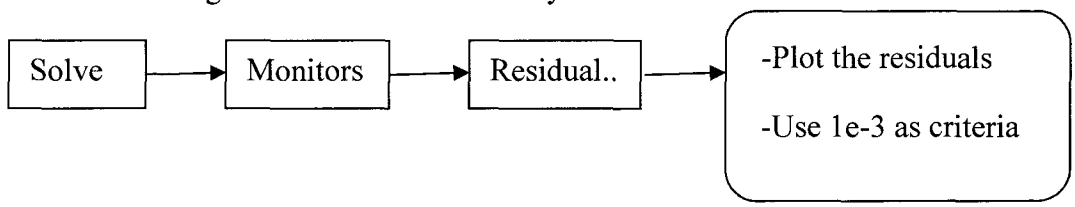

10. Obtain and monitor required data.

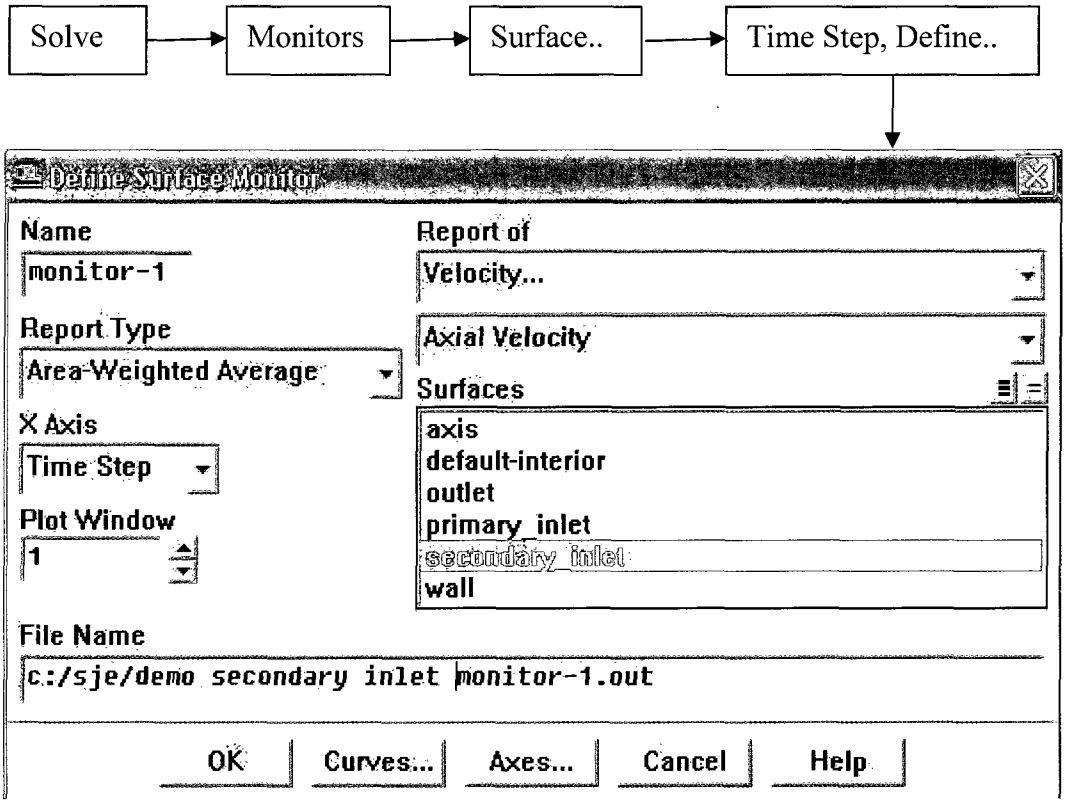

The area-averaged secondary inlet velocity is saved, for every time step, into a file in the specified folder. The same step can be applied to other surfaces.

11. Save data file and case file automatically.

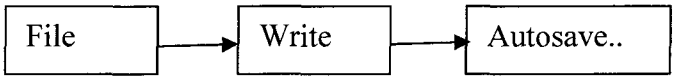

12. Start iteration.

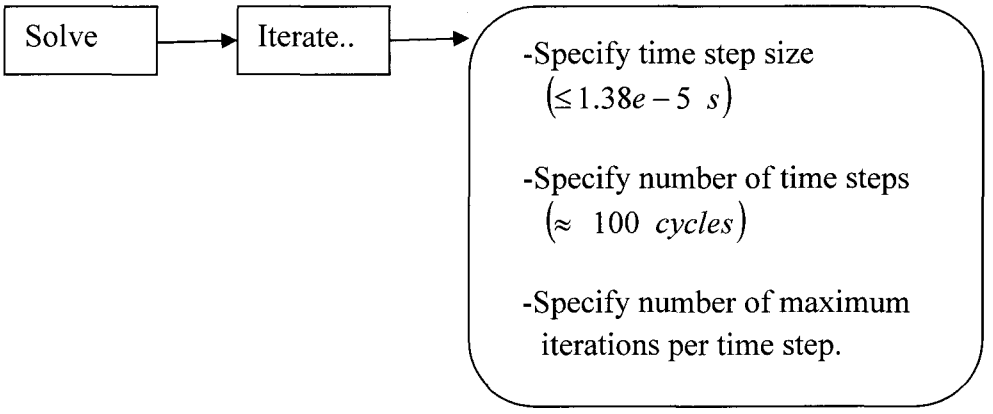

After the calculation is complete, the data file can be input to Excel for post-processing. If the 0.1% periodic state criterion is not met, more cycles need to be run until the periodic state is reached. All the Excel files for this study are included on the data CD.

Appendix D

Data Obtained From Fluent

The total size of all the data files is extremely large (over 100 GB). It is not practical to burn all the data on CDs. However, the Excel files with all important data are included on the single data CD. Their descriptions are given below.

- Aspectratio.xlsx: determine the cluster factor, f_a, for grid structure.
- Iterations.xlsx: SJE optimization iterations.
- Optimum performance.xlsx: final optimum SJE performance curve.
- sja validation.xlsx: SJ flow field and $k-\varepsilon$ model validations.
- sje2mmsofrquencystudy.xlsx: preliminary frequency study.
- sje2mmsogeometrystudy.xlsx: preliminary geometric study.
- sje2mmsopressurestudy.xlsx: preliminary pressure study.
- sje2mmsotimestepstudy.xlsx: preliminary time step size study
- sje2mmsovelocity.xlsx: preliminary velocity amplitude study.
- sje2mmtimeperiodic.xlsx: time periodic state study.
- sjeUDFcode.txt: UDF code for primary inlet velocity function, $V_p(t) = V_A \sin(2\pi f t)$.

REFERENCES

1. **Eiliat, H.**, *Experimental Study of Synthetic Jets,* Master's Thesis, 2009, Department of Mechanical, Automotive and Materials Engineering, University of Windsor, Canada.

2. FLUENT 6.3 User's Guide, Lebanon, NH, USA, 2006 (ANSYS Inc.).

3. **Fugal, S.R.,** *A Numerical Study of Oscillating Flow Through a Sudden Expansion,* Master's Thesis, 2004, Department of Mechanical and Aerospace Engineering, Utah State University, USA.

4. **Glezer, A. and Amitay, M.,** Synthetic Jets, Annual Review of Fluid Mechanics, 2002, 34: p. 503-529.

5. **Hill, B.J.,** Measurement of Local Entrainment Rate in the Initial Region of Axisymmetric Turbulent Air Jets, Journal of Fluid Mechanics, 1972, 51: p. 773-779.

6. **King, A.J.C. and Jagannatha, D.,** Simulation of Synthetic Jets with Non-Sinusoidal Forcing Functions for Heat Transfer Application, Proceedings of the 18th World IMACS/MODSIM Congress, Cairns, Australia, 2009: p. 1732-1738.

7. **Kral, L.D., Donovan, J.F., Gain, A.B. and Cary, A.W.,** Numerical Simulation of Synthetic Jet Actuators, AIAA Paper 97-1824, 28th AIAA Fluid Dynamics Conference, 4th AIAA Shear Flow Control Conference, 1997, Snowmass Village, CO, USA.

8. **Lee, C.Y. and Goldstein, D.B.,** Two-Dimensional Synthetic Jet Simulation, AIAA Journal, March 2002, 40(3): p. 510-516.

9. **Luo, Z.B., Xia, Z.X. and Liu, B.,** An Adjustable Synthetic Jet by a Novel PZT-Driven Actuator with a Slide Block, Journal of Physics, Conference Series, 2006, 34: p. 487-492.

10. **Mahalingam, R.,** Modeling of Synthetic Jet Ejectors for Electronics Cooling, 23rd IEEE SEMI-THERM Symposium, 2007, San Jose, CA, USA.

11. **Mallinson, S.G., Hong, G. and Reizes, J.A.,** Some Characteristics of Synthetic Jets, AIAA Paper 99-3651, 30th AIAA Fluid Dynamics Conference, 1999, Norfolk, VA, USA.

12. **Meng, G.C.,** *Air Ejector Pumping Enhancement Using Pulsed Primary Flow,* PhD Dissertation, 2005, Department of Mechanical and Manufacturing Engineering, University of Calgary, Canada.

13. **Munson, B.R., Young, D.F. and Okiishi, T.H.,** *Fundamental of Fluid Mechanics,* Fifth Edition, 2006, John Wiley & Sons, Inc., New York, NY, USA.

14. **Rampunggoon, P.,** *Interaction of a Synthetic Jet with a Flat Plate Boundary Layer,* PhD Dissertation, 2001, Department of Mechanical Engineering, University of Florida, FL, USA.

15. **Ravi, B.R. and Mittal, R.,** Numerical Study of Large Aspect-Ratio Synthetic Jets, AIAA Paper 2006-315, 44th AIAA Aerospace Science Meeting and Exhibit, 2006, Reno, NV, USA.

16. **Ricou, F.P. and Spalding, D.B.,** Measurements of Entrainment by Axisymmetrical Turbulent Jets, Journal of Fluid Mechanics, 1961, 11: p. 21-32.

17. **Rizzetta, D.P., Visbal, M.P. and Stanek, M.J.,** Numerical Investigation of Synthetic Jet Flowfields, AIAA Journal, 1999, 37: p. 919-927.

18. **Shih, C.,** Jet Flow Field, http://www.eng.fsu.edu/~shih/succeed/jet/jet.htm, [Accessed in August 2009]

19. **Shuster, J.M. and Smith, D.R.,** Experimental Study of the Formation and Scaling of A Round Synthetic Jet, Physics of Fluids, 2007, 19(4): p. 045109(1)-045109(21)

20. **Smith, B.L. and Swift, G.W.,** A Comparison Between Synthetic Jets and Continuous Jets, Experiments in Fluids, 2003, 34: p. 467-472.

21. **Smith, B.L., Trautman, M.A., and Glezer, A.,** The Formation and Evolution of Synthetic Jets, Physics of Fluids, 1998, 10: p. 2281-2297.

22. **Stoecker, W. F.,** *Design of Thermal System,* 1971, McGraw-Hill, New York, NY, USA.

23. **Utturkar, Y., Holman, R., Mittal, R., Carroll, B., Sheplak, M. and Cattafesta, L.,** A Jet Formation Criterion for Synthetic Jet Actuators, AIAA Paper 2003-0636, 41st AIAA Aerospace Science Meeting and Exhibit, 2003, Reno, NV, USA.

24. **Utturkar, Y., Mittal, R., Rampunggoon, P. and Cattafesta, L.,** Sensitivity of Synthetic Jets to the Design of the Jet Cavity, AIAA Paper 2002-0124, 40th AIAA Aerospace Science Meeting and Exhibit, 2002, Reno, NV, USA.

25. **Wilcox, D.C.,** *Turbulence Modeling for CFD,* 1998, DCW Industries Inc., La Canada, CA, USA.

26. **Vermeulen, P.J., Rainville, P. and Ramesh, V.,** Measurement of the Entrainment Coefficient of Acoustically Pulsed Axisymmetric Free Air Jets, Journal of Engineering for Gas Turbines and Power, 1992, 114: p. 409-415.

27. **Vermeulen, P.J., Ramesh, V. and Meng, G.C.,** Air Ejector Pumping Enhancement Through Pulsing Primary Flow, AIAA Paper 2004-2621, 2nd AIAA Flow Control Conference, 2004, Portland, OR, USA..

VITA AUCTORIS

Feng Lin was born in 1973 in Zhong Shan, Guang Dong, the People's Republic of China. He finished his high school education at Zhong Shan Oversea High School in 1992 in Zhong Shan. Feng immigrated to Canada with his family in the same year and attended J. L. Forster Secondary School in Windsor where he received his Ontario high school diploma in 1993. He then entered the University of Windsor for his postsecondary study in 1994, and graduated with an Honours Bachelor Degree in Applied Science in Mechanical Engineering in 1997. Feng joined the University of Windsor in 2006 for his graduate study. He is currently pursuing his Master of Applied Science degree in the Department of Mechanical, Automotive and Materials Engineering with specialization in Fluid Mechanics and hopes to graduate in September 2009.